Mon. Not. R. Astron. Soc. **354,** 558–574 (2004) doi:10.1111/j.1365-2966.2004.08218.x

Observations and three-dimensional photoionization modelling of the Wolf–Rayet planetary nebula NGC 1501

B. Ercolano,[1⋆] R. Wesson,[1] Y. Zhang,[2] M. J. Barlow,[1] O. De Marco,[3] T. Rauch[4,5] and X.-W. Liu[2]

[1]*Department of Physics and Astronomy, University College London, Gower St, London WC1E 6BT*
[2]*Department of Astronomy, Peking University, Beijing 100871, China*
[3]*Department of Astrophysics, American Museum of Natural History, Central Park West at 79th Street, NY 10024, USA*
[4]*Institut für Astronomie und Astrophysik, Abt. Astronomie, Sand 1, Universität Tübingen, 72076 Tübingen, Germany*
[5]*Dr-Remeis-Sternwarte, Sternwartstraße 7, D-96049 Bamberg, Germany*

Accepted 2004 July 12. Received 2004 July 2; in original form 2004 March 5

ABSTRACT

Deep optical spectra of the high-excitation planetary nebula NGC 1501 and its W04 central star are presented. A recombination line abundance analysis of the emission-line spectrum of the central star yields He : C : O mass fractions of 0.36 : 0.48 : 0.16, similar to those of PG 1159 stars. A detailed empirical analysis of the nebular collisionally excited line (CEL) and optical recombination line (ORL) spectrums are presented, together with fully three-dimensional photoionization modelling of the nebula. We found very large ORL–CEL abundance discrepancy factors (ADFs) for O^{2+} (32) and Ne^{2+} (33). The mean value of ∼5100 K for the T_e derived from He I recombination lines ratios is 6000 K, lower than the value of 11 100 K implied by the [O III] line ratio. This result indicates the existence of a second, low-temperature nebular component, which could account for the observed ORL emission. Electron temperature fluctuations (t^2) cannot account for the high ADFs found from our optical spectra of this nebula.

A three-dimensional photoionization model of NGC 1501 was constructed using the photoionization code MOCASSIN, based on our new spectroscopic data and using the three-dimensional electron density distribution determined from long-slit echellograms of the nebula by Ragazzoni et al. The central star ionizing radiation field is approximated by a model atmosphere, calculated using the Tübingen non-local thermodynamic equilibrium model atmosphere package, for abundances typical of the W04 nucleus of NGC 1501 and PG 1159 stars. The nebular emission-line spectrum was best reproduced using a central star model with an effective temperature of $T_{\rm eff} = 110$ kK and a luminosity of $L_* = 5000\,{\rm L}_\odot$. The initial models showed higher degrees of ionization of heavy elements than indicated by observations. We investigated the importance of the missing low-temperature dielectronic recombination rates for third-row elements and have estimated upper limits to their rate coefficients.

Our single-phase, three-dimensional photoionization model heavily underpredicts the optical recombination line emission. We conclude that the presence of a hydrogen-deficient, metal-rich component is necessary to explain the observed ORL spectrum of this object. The existence of such knots could also provide a softening of the radiation field, via the removal of ionizing photons by absorption in the knots, thereby helping to alleviate the overionization of the heavy elements in our models.

Key words: atomic data – stars: Wolf–Rayet – ISM: abundances – planetary nebulae: individual: NGC 1501.

1 INTRODUCTION

The high-excitation, northern planetary nebula (PN) NGC 1501 has been the subject of several recent tomographic and

⋆E-mail: be@star.ucl.ac.uk

spatio-kinematical studies (Sabbadin & Hamzaoglu 1982; Sabbadin et al. 2000a; Ragazzoni et al. 2001). The central star of NGC 1501 has been classified as O VI/WC4/WO4 (Aller 1976; Tylenda, Acker & Stenholm 1993; Gorny & Stasinska 1995; Crowther, de Marco & Barlow 1998), and has also been the subject of several studies, particularly as it is one of the few known pulsating PG 1159-type PN nuclei (Bond & Ciardullo 1993; Bond et al. 1996; Ciardullo & Bond 1996). A detailed study of the ionized nebular gas, has, however, not been carried out to date, due to the lack of suitable spectroscopic observations. In this paper we present a spectroscopic analysis and three-dimensional (3D) photoionization modelling of the ionized gas in NGC 1501. Based on new optical observations and using the three-dimensional photoionization code MOCASSIN (Ercolano et al. 2003a) and the density distribution derived by Ragazzoni et al. (2001), we construct models in order to obtain better constraints on the nebular physical properties and elemental abundances.

It is a well known and widely studied problem that optical recombination lines (ORLs) in gaseous nebulae yield higher empirical abundances than collisionally excited lines (CELs; for a recent review see Liu 2002); this is tightly correlated with Balmer jump (BJ) temperatures, T_e(BJ), being systematically lower than those from the [O III] nebular to auroral line ratio (Liu & Danziger 1993). One possible solution to the problem is that temperature and density fluctuations within the nebular gas lead to underestimated elemental abundances from standard CEL analyses (Peimbert 1967, 1971). While this may be a valid explanation for objects with low abundance discrepancy factors (e.g. Peimbert et al. 2004), for cases where T_e(BJ) is more than a factor of 2 lower than T_e([O III]) the method is no longer applicable (Liu 2002). Moreover, the t^2 values derived from T_e(BJ) and T_e([O III]) for some less extreme nebulae are found to be too small to reconcile the ORL and CEL abundances (Liu 2002). The main problem encountered with the t^2 formulation is the fact that the T_e-insensitive infrared (IR) fine-structure lines also yield much lower ionic abundances than those implied by ORLs (e.g. Rubin 1968; Liu et al. 2000, 2001a,b; Tsamis et al. 2004). The presence of hydrogen-deficient metal-rich knots of high density embedded in the normal nebular gas has been proposed as an alternative to temperature fluctuations for the case of the PN NGC 6153 (Liu et al. 2000). Dual abundance photoionization models have been constructed for PNe NGC 6153 (Péquignot et al. 2003; Tylenda 2003), M1-42 and M2-36 (Tylenda 2003) and for the hydrogen deficient knots of Abell 30 (Ercolano et al. 2003b). As discussed later in this paper, temperature and density fluctuations in a chemically homogeneous medium are not sufficient to explain the ionic abundance discrepancy factors (ADFs) derived from our observations of NGC 1501.

The new observational data are presented in Section 2, followed by a detailed empirical analysis of the ORL and CEL data, which is presented in Section 3. In that section we also carry out a study of the central star spectrum, providing identifications and measured equivalent widths of the detected stellar emission lines, and an abundance analysis for the central star wind. The three-dimensional photoionization modelling procedures are set out in Section 4, while Section 5 is concerned with the results of the modelling. After an investigation of the applicability of the t^2 formalism to our results, carried out in Section 6, there follows a discussion of how the presence of hydrogen-deficient, metal-rich knots could resolve the remaining discrepancies between ORL and CEL abundances as well as the overionization of the nebular gas as predicted by the modelling. Our final conclusions are given in Section 7 of the paper.

2 OBSERVATIONS

In this section new observations of the optical spectrum of NGC 1501 are presented. The nebular analysis and the three-dimensional modelling that follow are all based on the new data. The *International Ultraviolet Explorer* (*IUE*) spectra for the PN central star were also retrieved from the archive to provide some indication of the stellar energy distribution. These are also briefly discussed in this section.

2.1 Optical observations of NGC 1501

The observations were carried out in dark sky conditions on the night of 2003 August 1, using the double-armed ISIS long slit spectrograph mounted on the 4.2-m William Herschel Telescope at the Observatorio del Roque de los Muchachos, La Palma, Spain. The gratings used were the R316R in the red and the R600B in the blue, giving wavelength coverage from 3400 to 5100 Å in the blue and from 5100 to 8000 Å in the red. The spectrograph slit was aligned north–south, and the slit width used was 0.75 arcsec (the slit length was 4 arcmin), giving a spectral resolution of 1.5-Å full width half maximum (FWHM) in the blue and 2.8-Å FWHM in the red. Five exposure were taken, of 1800 s each.

The data were reduced using standard LONG92 procedures in MIDAS. The two-dimensional (2D) frames were bias-subtracted, flat-fielded and cleaned of cosmic rays. They were wavelength-calibrated using exposures of a CuNe+CuAr calibration lamp. Spectra were flux-calibrated using wide slit (8-arcsec) observations of the standard stars HZ44 and Feige 110. Unfortunately, wide slit observations of NGC 1501 were not acquired and, as a result, absolute flux calibration of its central star could not be carried out.

The top and bottom panels of Fig. 1 show the extracted blue and red spectra of NGC 1501 after integration over ∼68 arcsec (338 pixels) along the slit.

2.2 IUE observations of NGC 1501

Low- and high-dispersion ultraviolet spectra are available for NGC 1501 from the *IUE* archive. These have already been described by Feibelman (1998). Only the low-dispersion data are useful as the high-dispersion spectrum seems to be very underexposed. Moreover, as noted by Feibelman (1998), the nebular contribution to the *IUE* data is very small, as indicated by the weakness of the C III] λλ1906,1908 emission doublet, which is normally one of the major nebular emission features. Therefore, the *IUE* spectra could not be used for the nebular analysis carried out in this work. Nevertheless, the retrieved *IUE* SWP28953 and LWP08948 spectra were useful in providing some constraint on the luminosity of the central star, as described in Section 4.4.

3 EMPIRICAL ANALYSIS

3.1 The nebular spectrum

A full list of observed lines and their measured fluxes is presented in Table 1. All line fluxes, except those of the strongest lines, were measured using Gaussian line profile fitting. The fluxes of the strongest isolated lines were obtained by integration over the detected profile. Column 1 of Table 1 gives the observed wavelengths corrected for the heliocentric radial velocity of the nebula as determined from the

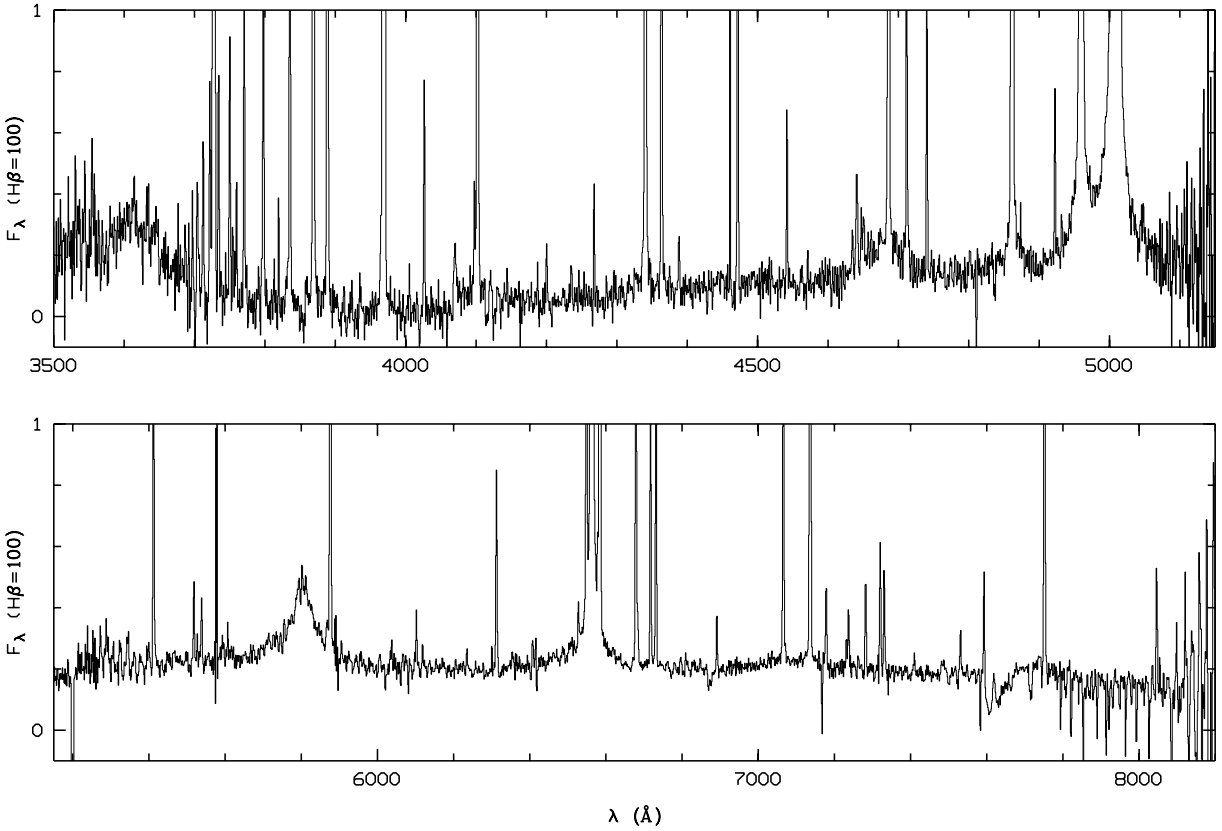

Figure 1. The observed optical spectrum of the PN NGC 1501 integrated over the angular extent of the nebula (68 arcsec) and normalized such that F(Hβ) = 100.

Table 1. Observed and dereddened relative line fluxes, on a scale where Hβ = 100. The integrated observed H(β) flux from Cahn et al. (1992) was dereddened using $c(H\beta) = 1.0$ to give an integrated dereddened flux of $I(H\beta) = 5.26 \times 10^{-11}$ erg s^{-1} cm^{-2}.

λ_{obs} (1)	$F(\lambda)$ (2)	$I(\lambda)$ (3)	Ion (4)	λ_{lab} (5)	Mult (6)	Lower term (7)	Upper term (8)	g_1 (9)	g_2 (10)
3614.02	0.56	1.07	He I	3613.64	V6	2s 1S	5p 1P*	1	3
3686.90	0.39	0.71	H 19	3686.83	H19	2p+ 2P*	19d+ 2D	8	*
3691.80	0.34	0.63	H 18	3691.56	H18	2p+ 2P*	18d+ 2D	8	*
3697.14	0.74	1.35	H 17	3697.15	H17	2p+ 2P*	17d+ 2D	8	*
3703.88	1.15	2.09	H 16	3703.86	H16	2p+ 2P*	16d+ 2D	8	*
3706.55	0.45	0.83	He I	3705.02	V25	2p 3P*	7d 3D	9	15
	*	*	O III	3707.25	V14	3p 3P	3d 3D*	3	5
3712.21	1.43	2.60	H 15	3711.97	H15	2p+ 2P*	15d+ 2D	8	*
3721.85	1.78	3.22	H 14	3721.94	H14	2p+ 2P*	14d+ 2D	8	*
	*	*	[S III]	3721.63	F2	3p2 3P	3p2 1S	3	1
3726.00	6.73	12.16	[O II]	3726.03	F1	2p3 4S*	2p3 2D*	4	4
3728.75	5.59	10.08	[O II]	3728.82	F1	2p3 4S*	2p3 2D*	4	6
3734.18	1.77	3.18	H 13	3734.37	H13	2p+ 2P*	13d+ 2D	8	*
3750.04	2.03	3.64	H 12	3750.15	H12	2p+ 2P*	12d+ 2D	8	*
3754.65	0.74	1.32	O III	3754.69	V2	3s 3P*	3p 3D	3	5
3759.64	0.98	1.74	O III	3759.87	V2	3s 3P*	3p 3D	5	7
3770.49	2.38	4.22	H 11	3770.63	H11	2p+ 2P*	11d+ 2D	8	*
3773.90	0.33	0.59	O III	3774.02	V2	3s 3P*	3p 3D	3	3
3777.82	0.16:	0.28	Ne II	3777.14	V1	3s 4P	3p 4P*	2	4
3791.08	0.36	0.63	O III	3791.27	V2	3s 3P*	3p 3D	5	5
3797.84	3.25	5.70	H 10	3797.90	H10	2p+ 2P*	10d+ 2D	8	*
3812.97	0.35	0.62	He II	3813.50	4.19	4f+ 2F*	19g+ 2G	32	*
3819.55	0.63	1.10	He I	3819.62	V22	2p 3P*	6d 3D	9	15
3835.36	4.77	8.23	H 9	3835.39	H9	2p+ 2P*	9d+ 2D	8	*
3858.14	0.24:	0.42	He II	3858.07	4.17	4f+ 2F*	17g+ 2G	32	*
3868.76	59.20	100.6	[Ne III]	3868.75	F1	2p4 3P	2p4 1D	5	5
3881.59	0.22	0.37	O II	3882.19	V12	3p 4D*	3d 4D	8	8

Table 1 – *continued*

λ_{obs} (1)	$F(\lambda)$ (2)	$I(\lambda)$ (3)	Ion (4)	λ_{lab} (5)	Mult (6)	Lower term (7)	Upper term (8)	g_1 (9)	g_2 (10)
	*	*	O II	3882.45	V11	3p 4D*	3d 4P	4	4
	*	*	O II	3883.13	V12	3p 4D*	3d 4D	8	6
3888.88	11.20	18.85	H 8	3889.05	H8	2p+ 2P*	8d+ 2D	8	*
	*	*	He I	3888.65	V2	2s 3S	3p 3P*	3	9
3923.65	0.15	0.25	He II	3923.48	4.15	4f+ 2F*	15g+ 2G	32	*
3967.58	17.30	28.12	[Ne III]	3967.46	F1	2p4 3P	2p4 1D	3	5
3970.26	10.60	17.19	H 7	3970.07	H7	2p+ 2P*	7d+ 2D	8	98
4026.37	1.51	2.38	He I	4026.21	V18	2p 3P*	5d 3D	9	15
4036.23	0.12:	0.19	N II	4035.08	V39a	3d 3F*	4f 2[4]	5	7
4070.16	0.96	1.49	[S II]	4068.60	F1	2p3 4S*	2p3 2P*	4	4
4076.22	0.21	0.32	[S II]	4076.35	F1	2p3 4S*	2p3 2P*	2	4
4097.95	1.15	1.75	N IIII	4097.33	V1	3s 2S	3p 2P*	2	4
4102.11	19.50	29.65	H 6	4101.74	H6	2p+ 2P*	6d+ 2D	8	72
4120.53	0.40	0.59	He I	4120.84	V16	2p 3P*	5s 3S	9	3
4144.12	0.20	0.29	He I	4143.76	V53	2p 1P*	6d 1D	3	5
4187.46	0.19	0.28	C III	4186.90	V18	4f 1F*	5g 1G	7	9
4200.23	0.41	0.60	He II	4199.83	4.11	4f+ 2F*	11g+ 2G	32	*
	*	*	N III	4200.10	V6	3s′ 2P*	3p′ 2D	4	6
4267.56	0.764	1.064	C II	4267.15	V6	3d 2D	4f 2F*	10	14
4285.32	0.13	0.19	O II	4285.69	V78b	3d 2F	4f F3*	6	8
4306.65	0.11	0.15	O II	4307.23	V53b	3d 4P	4f D2*	2	4
4340.79	35.90	48.09	H 5	4340.47	H5	2p+ 2P*	5d+ 2D	8	50
4357.68	0.29	0.45	O II	4357.25	V63a	3d 4D	4f D3*	6	8
	*	*	O II	4357.25	V63a	3d 4D	4f D3*	6	6
4363.53	7.86	10.39	[O III]	4363.21	F2	2p2 1D	2p2 1S	5	1
4367.55	0.30	0.40	O II	4366.89	V2	3s 4P	3p 4P*	6	4
4388.28	0.45	0.58	He I	4387.93	V51	2p 1P*	5d 1D	3	5
4397.42	0.08	0.11	Ne II	4397.99	V57b	3d 4F	4f 1[4]*	6	8
4409.66	0.09:	0.11	Ne II	4409.30	V55e	3d 4F	4f 2[5]*	8	10
4413.43	0.12	0.16	Ne II	4413.22	V65	3d 4P	4f 0[3]*	6	8
	*	*	Ne II	4413.11	V57c	3d 4F	4f 1[3]*	4	6
	*	*	Ne II	4413.11	V65	3d 4P	4f 0[3]*	6	6
4430.71	0.11:	0.14	Ne II	4430.94	V61a	3d 2D	4f 2[4]*	6	8
4457.24	0.10:	0.12	Ne II	4457.05	V61d	3d 2D	4f 2[2]*	4	6
	*	*	Ne II	4457.24	V61d	3d 2D	4f 2[2]*	4	4
4471.74	3.02	3.76	He I	4471.50	V14	2p 3P*	4d 3D	9	15
4477.54	0.09:	0.11	O II	4477.90	V88	3d 2P	4f G3*	4	6
4480.86	0.05:	0.06	Mg II	4481.21	V4	3d 2D	4f 2F*	10	14
4487.70	0.13	0.16	O II	4487.72	V104	3d′ 2P	4f′ D2*	2	4
	*	*	O II	4488.20	V104	3d′ 2P	4f′ D2*	4	6
4510.48	0.15	0.18	N III	4510.91	V3	3s′ 4P*	3p′ 4D	4	6
	*	*	N III	4510.91	V3	3s′ 4P*	3p′ 4D	2	4
4541.75	1.04	1.24	He II	4541.59	4.9	4f+ 2F*	9g+ 2G	32	*
4563.02	0.16	0.19	Mg I]	4562.60		3s2 1S	3s3p 3P*	1	5
4571.23	0.19	0.23	Mg I]	4571.10		3s2 1S	3s3p 3P*	1	3
4610.34	0.11:	0.13	O II	4610.20	V92c	3d 2D	4f F2*	4	6
4613.89	0.11	0.13	N II	4613.87	V5	3s 3P*	3p 3P	3	3
	*	*	O II	4613.14	V92b	3d 2D	4f F3*	6	6
	*	*	O II	4613.68	V92b	3d 2D	4f F3*	6	8
4621.17	0.087	0.10	N II	4621.39	V5	3s 3P*	3p 3P	3	1
4634.66	0.51	0.58	N III	4634.14	V2	3p 2P*	3d 2D	2	4
4640.97	1.18	1.34	N III	4640.64	V2	3p 2P*	3d 2D	4	6
4647.17	0.49	0.56	C III	4647.42	V1	3s 3S	3p 3P*	3	5
4650.76	0.80	0.91	C III	4651.47	V1	3s 3S	3p 3P*	3	1
4657.12	0.20	0.22	[Fe III]	4658.10	F3	3d6 5D	3d6 3F2	9	9
	*	*	C IV	4658.30		5	6		
4661.37	0.29	0.45	O II	4661.63	V1	3s 4P	3p 4D*	4	4
4685.99	36.50	40.30	He II	4685.68	3.4	3d+ 2D	4f+ 2F*	18	32
4697.10	0.13	0.14	O II	4696.35	V1	3s 4P	3p 4D*	6	4
4711.72	2.44	2.66	[Ar IV]	4711.37	F1	3p3 4S*	3p3 2D*	4	6
4740.52	1.87	2.00	[Ar IV]	4740.17	F1	3p3 4S*	3p3 2D*	4	4
4861.84	100.0	100.0	H 4	4861.33	H4	2p+ 2P*	4d+ 2D	8	32
4881.24	0.061	0.060	[Fe III]	4881.11	F2	3d6 5D	3d6 3H	9	9

Table 1 – *continued*

λ_{obs} (1)	$F(\lambda)$ (2)	$I(\lambda)$ (3)	Ion (4)	λ_{lab} (5)	Mult (6)	Lower term (7)	Upper term (8)	g_1 (9)	g_2 (10)
4922.45	1.11	1.07	He I	4921.93	V48	2p 1P*	4d 1D	3	5
4932.05	0.37	0.35	[O III]	4931.80	F1	2p2 3P	2p2 1D	1	5
4959.47	416.0	393.6	[O III]	4958.91	F1	2p2 3P	2p2 1D	3	5
5007.30	1250.	1151.	[O III]	5006.84	F1	2p2 3P	2p2 1D	5	5
5199.15	0.930	0.77	[N I]	5199.84	F1	2p3 4S*	2p3 2D*	4	4
	*	*	[N I]	5200.26	F1	2p3 4S*	2p3 2D*	4	6
5412.04	5.01	3.68	He II	5411.52	4.7	4f+ 2F*	7g+ 2G	32	98
5453.01	0.21:	0.15	S II	5453.83	V6	4s 4P	4p 4D*	6	8
5518.04	1.09	0.76	[Cl III]	5517.66	F1	2p3 4S*	2p3 2D*	4	6
5538.04	1.04	0.72	[Cl III]	5537.60	F1	2p3 4S*	2p3 2D*	4	4
5666.98	0.19	0.12	N II	5666.63	V3	3s 3P*	3p 3D	3	5
5674.72	0.23	0.15	N II	5676.02	V3	3s 3P*	3p 3D	1	3
5755.87	0.39	0.25	[N II]	5754.60	F3	2p2 1D	2p2 1S	5	1
5802.58	0.71	0.45	C IV	5801.51	V1	3s 2S	3p 2P*	2	4
5811.60	0.72	0.45	C IV	5812.14	V1	3s 2S	3p 2P*	2	2
5876.14	18.70	11.40	He I	5875.66	V11	2p 3P*	3d 3D	9	15
6037.34	0.53	0.31	He II	6036.70	5.21	5g+ 2G	21h+ 2H*	50	*
6074.27	0.37	0.21	He II	6074.10	5.20	5g+ 2G	20h+ 2H*	50	*
6102.35	0.76	0.43	[K IV]	6101.83	F1	3p4 3P	3d4 1D	5	5
6118.58	0.52	0.29	He II	6118.20	5.19	5g+ 2G	19h+ 2H*	50	*
6235.04	0.40	0.21	He II	6233.80	5.17	5g+ 2G	17h+ 2H*	50	*
6300.45	0.27	0.14	[O I]	6300.34	F1	2p4 3P	2p4 1D	5	5
6312.51	2.85	1.48	[S III]	6312.10	F3	2p2 1D	2p2 1S	5	1
	*	*	He II	6310.80	5.16	5g+ 2G	16h+ 2H*	50	*
6393.54	0.13	0.07	[Mn V]	6393.60		3d3 4F	3d3 4P	10	6
6407.79	0.48	0.24	He II	6406.30	5.15	5g+ 2G	15h+ 2H*	50	*
6527.78	0.60	0.29	He II	6527.11	5.14	5g+ 2G	14h+ 2H*	50	*
6548.69	6.57	3.16	[N II]	6548.10	F1	2p2 3P	2p2 1D	3	5
6563.26	665.0	318.3	H 3	6562.77	H3	2p+ 2P*	3d+ 2D	8	18
6583.95	20.90	9.93	[N II]	6583.50	F1	2p2 3P	2p2 1D	5	5
6678.73	6.97	3.21	He I	6678.16	V46	2p 1P*	3d 1D	3	5
6717.04	3.90	1.77	[S II]	6716.44	F2	2p3 4S*	2p3 2D*	4	6
6731.42	4.31	1.95	[S II]	6730.82	F2	2p3 4S*	2p3 2D*	4	4
6795.87	0.28	0.12	[K IV]	6795.00	F1	3p4 3P	3p4 1D	3	5
6891.36	0.84	0.36	He I	6890.88	5.12	5g+ 2G	12h+ 2H	50	*
7065.82	6.12	2.51	He I	7065.25	V10	2p 3P*	3s 3S	9	3
7136.34	35.70	14.34	[Ar III]	7135.80	F1	3p4 3P	3p4 1D	5	5
7159.16	0.11	0.045	He I	7160.56		3s 3S	10p 3P*	3	9
7178.31	1.11	0.44	He II	7177.50	5.11	5g+ 2G	11h+ 2H*	50	*
7231.51	0.34	0.13	C II	7231.32	V3	3p 2P*	3d 2D	2	4
7237.20	0.92	0.36	C II	7236.42	V3	3p 2P*	3d 2D	4	6
	*	*	C II	7237.17	V3	3p 2P*	3d 2D	4	4
	*	*	[Ar IV]	7237.26	F2	3p3 2D*	3p3 2P*	6	4
7262.88	0.21	0.08	[Ar IV]	7262.76	F2	3p3 2D*	3p3 2P*	4	2
7282.00	1.42	0.55	He I	7281.35	V45	2p 1P*	3s 1S	3	1
7320.36	1.91	0.73	[O II]	7318.92	F2	2p3 2D*	2p3 2P*	6	2
	*	*	[O II]	7319.99	F2	2p3 2D*	2p3 2P*	6	4
7330.69	1.55	0.59	[O II]	7329.67	F2	2p3 2D*	2p3 2P*	4	2
	*	*	[O II]	7330.73	F2	2p3 2D*	2p3 2P*	4	4
	*	*	[Ar IV]	7331.40	F2	3p3 2D*	3p3 2P*	6	2
7531.01	0.72	0.26	[Cl IV]	7530.54		3p2 3P	3p2 1D	3	5
7592.85	1.28	0.45	He II	7592.74	5.10	5g+ 2G	10h+ 2H	5	*
7618.89	0.78	0.27	N V	7618.46	V13	7g+ 2G	8h+ 2H	*	*
7751.64	9.84	3.52	[Ar III]	7751.06		3p4 3P	3p4 1D	3	5
8046.37	1.70	0.54	[Cl IV]	8045.63		3p2 3P	3p2 1D	5	5

Balmer lines. The observed fluxes are given in column 2. Column 3 lists the fluxes after correction for interstellar extinction, according to $I(\lambda) = 10^{c(\mathrm{H}\beta)f(\lambda)}F(\lambda)$, where $f(\lambda)$ is the standard Galactic extinction law for a total-to-selective extinction ratio of $R = 3.1$ (Howarth 1983) and $c(H\beta)$ is the logarithmic extinction at Hβ (see Section 3.3). The ionic identification, laboratory wavelength, multiplet number, the lower- and upper-spectral terms of the transition, and the statistical weights of the lower and upper levels, are given in columns 4–10, respectively. All fluxes are given relative to Hβ, on a scale where H$\beta = 100$.

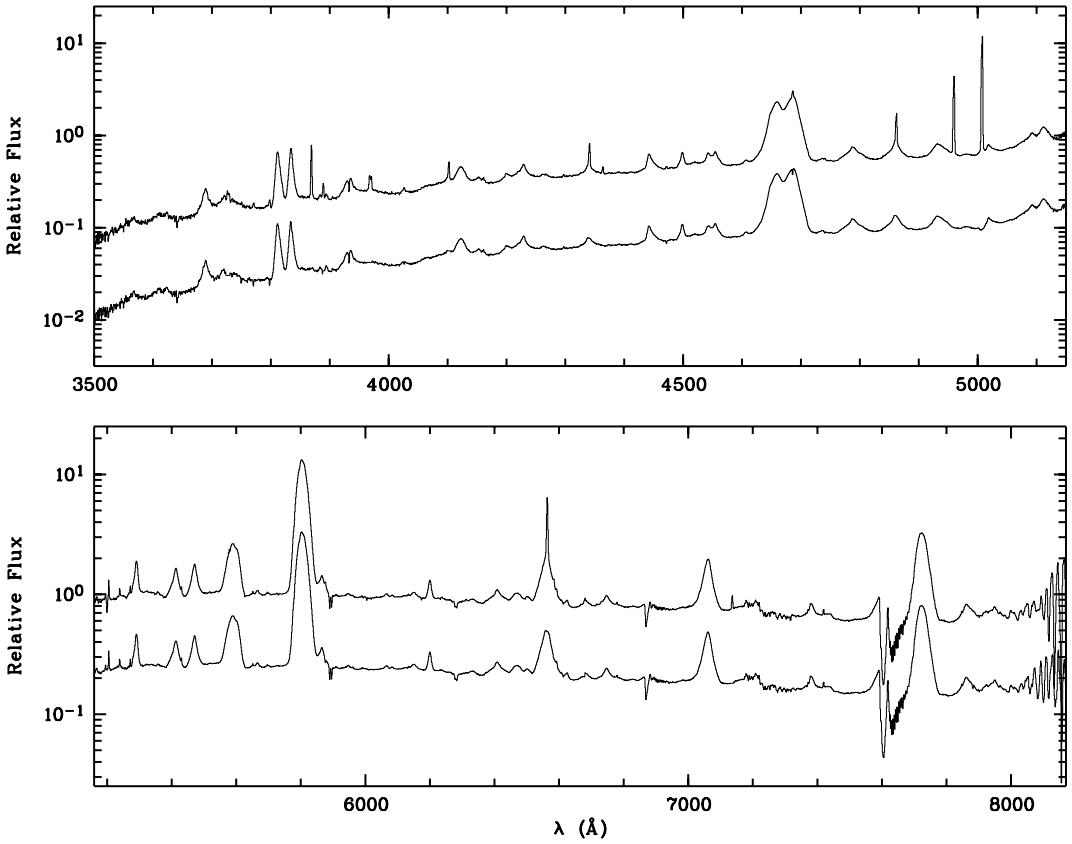

Figure 2. Observed optical spectrum of the central star. Each panel shows the spectrum detected in the centre of the slit (upper line) and the same spectrum after subtraction of the nebular spectrum (lower line). As a result of atmospheric dispersion effects on our narrow-slit spectrum, the slope of the stellar energy distribution is not reliable.

3.2 The central star spectrum

The upper and lower panels of Fig. 2 show the blue and red spectra measured at the central star position. In each panel the upper plot shows the unsubtracted spectrum and the lower shows the spectrum after subtraction of the nebular spectrum. The central star spectrum was integrated over 5.8 arcsec (30 pixels) along the slit, and the nebular spectrum subtracted from it was taken an equal area 10 arcsec (50 pixels) away from the central position. The figure shows that some emission lines have both a stellar and a nebular component, but most are only produced by one or the other. As expected, broadening of the stellar lines is evident, while the width of the detected nebular lines is much narrower.

Our 2.5-h exposure on the 14th magnitude central star of NGC 1501 with the ISIS spectrograph of the 4.2-m WHT, led to a very high signal-to-noise ratio spectrum. The stellar emission lines are relatively narrow for a star of its class, and so many lines could be identified. Emission lines from four ionization stages of oxygen (O V–O VIII), together with numerous C IV and He II lines, were found to be present. We detected a very weak C III 5696-Å emission feature, where the equivalent width (EW) of 0.40 Å was 1120 times weaker than that of the C IV 5801,12-Å doublet. Identifications and measured EWs for the stellar emission lines are listed in Table 2. Our EWs show quite good agreement with those measured for a subset of the lines by Stanghellini, Kaler & Shaw (1994), though we note that our ionic attributions for the lines at 3689, 3933, 4780, 4931, 5291 and 5471 Å differ from those of Stanghellini et al. Using the WO star classification criteria listed in table 3 of Crowther et al. 1998, the EWs listed in our Table 2 yield a spectral type of WO4, in agreement with the subtype assigned by Crowther et al. to this central star.

The airmass at the time of the observations was quite large (1.44–2.13), so that the effects of differential atmospheric dispersion on the narrow (0.75-arcsec) slit needed for the nebular ORL analysis led to significant losses towards the blue end of the central star spectrum. For this reason, neither the spectral slope nor the absolute continuum fluxes of the central star of NGC 1501 can be derived from the optical observations presented in this paper.

Despite the g-mode pulsations detected in the central star of NGC 1501 (Bond et al. 1996) the emission-line optical spectrum of this star (see Fig. 2) points towards the presence of a thick wind – no stellar absorption lines were detected at all. Koesterke & Hamann (1997) derived a mass-loss-rate of $5.2 \times 10^{-7}\,M_{\odot}\ yr^{-1}$ and a terminal stellar wind velocity of 1800 km s^{-1}, while Feibelman (1998) estimated the terminal stellar wind velocity to be in the 3260–3460 km s^{-1} range from its *IUE* low-resolution spectrum. Following the method of Kingsburgh, Barlow & Storey (1995), recently reviewed by Drew et al. (2004), we estimate the terminal stellar wind velocity by measuring the half width at zero intensity (HWZI) of the C IV λλ5801,12 doublet. Kingsburgh et al. (1995) showed that in the case of Sand 1, a SMC W03 star, the velocity corresponding to the HWZI of C IV λλ5801,12 doublet, corrected for the 10.65-Å doublet splitting, was consistent with the terminal wind velocity measured from the black absorption edge of the C IV λλ1548,51 resonance doublet, measured in a high-resolution *IUE* spectrum. The validity of the method was later confirmed for several other objects.

Table 2. Identifications and measured equivalent widths (EW) of emission features in the spectrum of the central star of NGC 1501. The EWs were derived after subtraction of the nebular spectrum.

λ_{obs} (Å)	EW (Å)	Ion	λ_{lab} (Å)	Lower term	Upper term
3566	1.5	C IV	3566.8	7	15
3620	3.8	C IV	3607.3	6p	9d
	*	O VI	3615.6	6p	7s
3689	7.9	C IV	3689.7	6	9
3723	11.2	C IV	3720.1	7	14
	*	O V	3698-3725	$3p'\,^3D$	$3d'\,^3D^o$
3811	24.5	O VI	3811.4	$3s\,^2S$	$3p\,^2P^\circ$
3834	21.2	O VI	3834.4	$3s\,^2S$	$3p\,^2P^\circ$
3933	11.0	C IV	3929.3	7	13
	*	C IV	3934.4	$5s\,^2S$	$6p\,^2P^\circ$
	*	O VI	3936.6	9	13
3976	5.0	?			
4026	0.70	He II	4025.6	4	13
4121	6.2	O V	4119-4124	$3s'\,^3P^\circ$	$3p'\,^3D$
4153	1.6	O V	4153.3	$3s'\,^3P^\circ$	$3p'\,^3D$
4161	*	C IV	4160.2	6p	12d
4199	1.26	He II	4199.8	4	11
4221	5.0	C IV	4219.0	$6s\,^2S$	$8p\,^2P^\circ$
4229	*	C IV	4229.1	7	12
4265	0.94	?			
4298	0.17	?			
4340	4.2	He II	4338.7	4	10
4412	0.23	?			
4442	6.8	C IV	4441.1	5p	6d
4479	0.14	O V	4479.5	$6g\,^3G$	$7h\,^3H$
4499	2.8	O VI	4499.0	8	10
4520	1.5	O VI	4521.2	7	9
4541	3.0	He II	4541.6	4	9
4554	4.0	C IV	4554.3	6p	8d
	*	O V	4554.5	$3p'\,^1P$	$3d'\,^1D$
4607	0.65	C IV	4604.6	7p	11d
4659	85	C IV	4658.7	5	6
4686	107	He II	4685.7	3	4
*	*	C IV	4685.4	6	8
*	*	C IV	4688.9	7	11
4736	0.60	C IV	4736.0	6d	8p
4780	9.8	O VI	4773.3	7s	8p
	*	C IV	4785.9	5d	6f
	*	C IV	4789.3	6p	8s
4861	9.1	He II	4859.3	4	8
	*	C IV	4860	8	16
4931	9.4	O V	4930.3	6h	7i
4981	0.66	O V	4977-4984	$6f\,^3F^o$	$7g\,^3G$
5018	3.1	C IV	5017.8	$5p\,^2P^\circ$	$6s\,^2S$
5092	13.0	C IV	5092.7	8	15
	*	O VI	5083.9	7p	8d
5114	*	O V	5114.1	$3s\,^1S$	$3p\,^1P^\circ$
5168	0.81	O VI	5166.7	10	14
5291	10.4	O VI	5290.6	7	8
5325-5358	1.9	C IV	5335.2	8p	14d
	*	C IV	5356.9	7p	10d
5413	15.1	He II	5411.5	4	7
	*	C IV	5411.0	8	14
5471	15.8	C IV	5470.7	7	10
5518-5538	0.95	C IV	5518.8	7p	10s
	*	C IV	5530.5	8s	13p
5591	65.5	O V	5572-5604	$3p\,^3P^\circ$	$3d\,^3D$
5651	0.58				
5667	1.05	O V	5668.8	9	13
	*	O VII	5669.3	8	9
5696	0.40	C III	5695.9	$3p\,^1P^\circ$	$3d\,^1D$
5806	448	C IV	5801.3,5812.0	$3s\,^2S$	$3p\,^2P^\circ$
5865	7.0	C IV	5865.4	8	13
5947	1.46	C IV	5946.9	9	19
6066	0.88	O VIII	6068.2	9	10
	*	O VIII	6064.2	11	13
6084	0.34	O VII	6085.1	10	12
6120	0.28	He II	6118.3	5	19
6136	0.36	O V	6131	$4s'\,^3P^o$	$4p'\,^3P$
6150-6170	1.9	C IV	6149.9	8s	12p
	*	He II	6170.7	5	18
6200	4.8	O VI	6200.8	9	11
*	*	O VI	6198.3	10	13
6235	0.46	He II	6233.8	5	17
6332	0.85	O V	6330.1	$3p'\,^1D$	$3d'\,^1F^o$
6408	8.4	C IV	6404.4	7s	9p
	*	C IV	6408.7	9	17
	*	He II	6406.4	5	15
6461	4.3	O V	6460,66	$3p\,^3D$	$3d\,^3F^\circ$
6502	1.35	O V	6500.2	$3p\,^3D$	$3d\,^3F^\circ$
6563	51.4	He II	6560.1	4	6
	*	C IV	6559.5	8	12
6624	1.2				
6682	2.4	He II	6683.2	5	13
6747	4.3	O V	6747.0	9	12
*	*	C IV	6747.5	9	16
7062	53.0	C IV	7062.4	7	9
7382	4.3	C IV	7380.4	6p	7d
7434	2.2	O V	7422-7443	$4s'\,^3S$	$4p'\,^3P^o$
7723	187	C IV	7726.4	6	7
*	*	C IV	7735.9	8	11
*	*	O VI	7717.1	8	9
7862	12.0	C IV	7860.7	9	14
7924	1.5	O VII	7926.4	9	10
7949	7.1	C IV	7947.2	6d	7p

We measured a full width at zero intensity (FWZI) of 103 Å for the C IV λλ5801,12 doublet, which, following the Kingsburgh et al. (1995) approach discussed above, yields a corrected HWZI of 46.2 Å and a terminal stellar wind velocity of 2390 km s^{-1} for the central star of NGC 1501.

3.3 Reddening

The logarithmic extinction at Hβ, $c(\mathrm{H}\beta) = \log[I(\mathrm{H}\beta)/F(\mathrm{H}\beta)]$, was derived from the Balmer line ratios, Hα/Hβ, Hγ/Hβ, Hδ/Hβ and Hϵ/Hβ. The measured ratios, together with the corresponding value of $c(\mathrm{H}\beta)$ are given in Table 3. The theoretical line ratios used were those given by Storey & Hummer (1995) for T_e = 11 kK and $N_e = 10^3$ cm^{-3} and we adopted the Galactic reddening law of Howarth (1983). Given the uncertainty introduced by the different flux calibrations for the two arms of the spectrograph, we expect large error bars on our measured Hα/Hβ ratio and on the corresponding value of $c(H\beta)$. We finally adopted the value $c(\mathrm{H}\beta) = 1.0$ as this best corrected the 2200-Å interstellar absorption feature. This value, which is used to correct observed fluxes for interstellar extinction throughout this work, is within the range of values reported in the literature for this object −0.96: Kaler (1976); 1.2: Cahn, Kaler & Stanghellini (1992); 1.1: Stanghellini et al. (1994); 1.11: Ciardullo & Bond (1996); 1.05: Sabbadin et al. (2000a).

Table 3. Logarithmic extinction coefficient derived from the Balmer decrement.

Balmer decrement	Ratio		$c(H\beta)$
	Theory[a]	Observed	
$H\alpha/H\beta$	2.837	6.65	1.15
$H\gamma/H\beta$	0.470	0.359	0.92
$H\delta/H\beta$	0.260	0.195	0.69
$H\eta/H\beta$	0.160	0.106	0.86
Adopted			1.0

[a]Theoretical line ratios are from Storey & Hummer (1995).

3.4 A recombination line abundance analysis for the WO4 central star

The WO4 central star of NGC 1501 has a pure emission-line spectrum and so we have used the recombination line method of (Kingsburgh et al. 1995 KBS95) to derive the relative abundances of helium, carbon and oxygen ions in its wind. For the case of the LMC WO3 star Sanduleak 2, Crowther et al. (2000) derived He, C and O abundances for its wind via spherical non-local thermodynamic equilibrium (NLTE) line-blanketed modelling, which showed good agreement with those derived from the recombination line analysis of KBS95, so we expect our recombination line abundances for the nucleus of NGC 1501 to be reliable.

To overcome the lack of a spectrophotometric calibration for our central star spectrum, we derived dereddened emission line fluxes by normalizing the equivalent widths listed in Table 2 to a continuum flux slope corresponding to the model atmospheres discussed in Sections 4.4 and 4.5. The $T_{\rm eff} = 110$ kK, $\log g = 6.0$ plane parallel NLTE Tübingen model discussed in Section 4.4 has a flux distribution between 4000 and 7000 Å, which can be approximated by $F_\lambda \propto \lambda^{-n}$, with $n = 3.93$, while the spherically symmetric CMFGEN model discussed in Section 4.5 has $n = 3.85$. We adopted a spectral slope of $n = 3.90$ and normalized it to $F_\lambda = 4.58 \times 10^{-14}$ erg cm^{-2} s^{-1} Å^{-1} at 5470 Å, corresponding to dereddening by $c(\mathrm{H}\beta) = 1.00$ the continuum-level V magnitude of 14.44 measured by Stanghellini et al. (1994). Column 3 of Table 4 lists the resulting dereddened line fluxes used for the abundance analysis, while column 4 lists the adopted line emission coefficients, Q ($= h\nu\alpha_{\rm rec}$), for $T_{\rm e} = 5 \times 10^4$ K and $N_{\rm e} = 10^{11}$ cm^{-3}, taken from table 14 of KBS95. Column 5 lists the ionic emission measures, I/Q, derived from each line, and mean I/Q values for each ion when more than one line was available. The C^{4+} emission measures derived from the four C IV recombination lines used for the abundance analysis show excellent agreement with each other. Their mean I/Q value was used to predict the fluxes of the various C IV lines that blend with the He II lines used for our analysis. After correcting for these blends, the I/Qs derived from the He II lines showed excellent interagreement.

Summing all ionic species, we find number ratios of C/He = 0.44, O/He = 0.107 and (C+O)/He = 0.55 for the central star of NGC 1501. These ratios are not dissimilar to the number ratios of C/He = 0.48 and O/He = 0.054 derived by Barlow & Hummer (1982) from a recombination line analysis of the WO1 PN central star Sanduleak 3. Expressed as mass fractions, we obtain He: C : O = 0.36 : 0.48 : 0.16 for the central star of NGC 1501, very similar to the values that have been derived from absorption-line analyses of pulsating PG 1159-type objects, stars that have been postulated to be the descendants of PN WC/WO central stars (see Werner, Heber & Hunger 1991).

Table 4. Wind abundance analysis for the central star of NGC 1501. Column 1 lists the recombining ion, column 2 lists the transition and column 3 lists the dereddened line flux obtained by normalizing the equivalent width listed in Table 2 to a stellar continuum that has a flux of $F_\lambda = 4.58 \times {}^{-14}$ erg cm^{-2} s^{-1} Å^{-1} at 5470 Å and a spectral slope corresponding to $F_\lambda \propto \lambda^{-3.90}$ (see the text). Column 4 lists the line recombination coefficient Q for $T_{\rm e} = 5 \times 10^4$ K and $N_{\rm e} = 10^{11}$ cm^{-3} (see Kingsburgh et al. 1995), while column 5 lists the derived ionic emission measure, I/Q. Values appearing in brackets are where He II line fluxes have been corrected for the contribution made by blended C IV lines, where use has been made of the mean I/Q derived for C^{4+}.

Recombining ion	Transition	I (erg cm^{-2} s^{-1})	Q (erg cm^3 s^{-1})	I/Q (cm^{-5})
C^{4+}	4658 (6→5)	7.29×10^{-12}	6.65×10^{-25}	1.096×10^{13}
	5471 (10→7)	7.21×10^{-13}	6.06×10^{-26}	1.195×10^{13}
	5801,12 ($3d^2P^o \rightarrow 3p^2S$)	1.626×10^{-11}	1.39×10^{-24}	1.169×10^{13}
	7062 (9→7)	8.96×10^{-13}	8.30×10^{-26}	1.080×10^{13}
	Mean C^{4+}			$1.135 \pm 0.05 \times 10^{13}$
He^{2+}	4686 (4→3)	8.96×10^{-12}		
		$\rightarrow 6.43 \times 10^{-12}$	2.38×10^{-25}	2.70×10^{13}
	[C^{4+} 4685 (8→6), 4689 (11→7)]	(2.53×10^{-12})	2.23×10^{-25}	(1.135×10^{13})
	5412 (7→4)	7.21×10^{-12}		
		$\rightarrow 5.47 \times 10^{-12}$	2.20×10^{-26}	2.49×10^{13}
	[C^{4+} 5411 (14→8)]	(1.74×10^{-13})	1.53×10^{-26}	(1.135×10^{13})
	6560 (6→4)	1.16×10^{-12}		
		$\rightarrow 8.40 \times 10^{-13}$	3.28×10^{-26}	2.56×10^{13}
	[C^{4+} 6560 (12→8)]	(3.20×10^{-13})	2.82×10^{-26}	(1.135×10^{13})
	Mean He^{2+}			$2.58 \pm 0.12 \times 10^{13}$
O^{5+}	4930 (7→6)	6.45×10^{-13}	8.53×10^{-25}	7.56×10^{11}
	5591 ($3d\ ^3D \rightarrow 3p\ ^3P^\circ$)	2.75×10^{-12}	4.33×10^{-24}	6.35×10^{11}
	Mean O^{5+}			$6.96 \pm 0.60 \times 10^{11}$
O^{6+}	5291 (8→7)	5.42×10^{-13}	1.05×10^{-24}	5.16×10^{11}
	6200 (11→9, 13→10)	1.35×10^{-13}	3.06×10^{-24}	4.41×10^{11}
	Mean O^{6+}			$4.77 \pm 0.37 \times 10^{11}$
O^{7+}	6085 (12→10)	1.028×10^{-14}	3.02×10^{-25}	3.40×10^{10}
O^{8+}	6068 (10→9), 6064 (13→11)	2.69×10^{-14}	1.72×10^{-24}	1.56×10^{10}

Table 5. Plasma diagnostics.

Ion	Lines	Ratio	Result
			$\log N_e$ (cm^{-3})[a]
[S II]	$I(\lambda6731)/I(\lambda6716)$	1.10	2.96
[O II]	$I(\lambda3729)/I(\lambda3726)$	0.83	3.00
[O II]	$I(\lambda3727)/I(\lambda7325)$	16.85	3.38
[Cl III]	$I(\lambda5537)/I(\lambda5517)$	0.95	3.22
[Ar IV]	$I(\lambda4740)/I(\lambda4711)$	0.75	2.77
			T_e (K)[b]
[N II]	$I(\lambda6548+\lambda6584)/I(\lambda5754)$	52.60	12 600
[O III]	$I(\lambda4959+\lambda5007)/I(\lambda4363)$	148.7	11 100
He I	$I(\lambda5876)/I(\lambda4471)$	3.03	4100
He I	$I(\lambda6678)/I(\lambda4471)$	0.86	5100
He I	$I(\lambda6678)/I(\lambda7281)$	5.88	4800
He I	$I(\lambda5876)/I(\lambda7281)$	20.84	6500
BJ/H 11		0.125	9400
			±3000

[a]Assuming $T_e = 11\,100$ K;
[b] Assuming $\log N_e(\mathrm{cm}^{-3}) = 3.0$.

3.5 Nebular empirical abundance determination

A number of CELs, which are useful as nebular N_e and T_e diagnostics, as well as for abundance determination, were detected in the spectra of NGC 1501. Using multilevel ($\geqslant$5) atomic models and solving the equations of statistical equilibrium, temperatures and densities were derived from these various CEL line ratios. The diagnostic line ratios and corresponding values of N_e and T_e are given in Table 5.

The [S II] ($\lambda6716/\lambda6731$), [O II] ($\lambda3729/\lambda3726$), [Cl III] ($\lambda5537/\lambda5517$) and [Ar IV] ($\lambda4740/\lambda4711$) diagnostic line ratios yield electron densities that are in good agreement with each other, giving an average density and standard error of (1040 ± 200) cm^{-3}. A higher density (2400 cm^{-3}) is derived from the [O II] ($\lambda3727/\lambda7325$) ratio. As a result of the higher critical density of the $\lambda\lambda$7320,30 doublet, the density derived from this diagnostic is weighted toward high-density regions of the nebula.

The [O III] nebular-to-auroral line ratio gives a temperature of 11.1 kK, which is slightly lower than the 12.6 kK given by the [N II] nebular-to-auroral ratio. Results from the photoionization modelling in Section 5 show that T_e([O III]) is almost equal to T_e([O II]) and T_e([N II]), and therefore the elevated temperatures measured from the [O II] and [N II] line ratios could be due to recombination excitation of the relevant CELs (Rubin 1986).

We calculated the contribution of recombination excitation to the [O II] λ7320,7330 and λ3727,3729 lines using equation (2) from Liu et al. (2000), and the relation $I_R(\lambda3727, 3729) = 7.7\, I_R(\lambda7320,7330)$ at 10 kK. Using the O^{2+}/H^+ abundance derived from CELs (see Section 3.6), the corrected 7325/3727 Å line ratio is 0.0514, giving a revised temperature of 13.7 kK, compared with the value of 16 200 K that is derived when no corrections are made.

Using the formalism of Liu et al. (2001b), we derived $T_e(\mathrm{BJ}) = 9.4$ kK from the ratio of the nebular continuum Balmer discontinuity at 3646 Å to H11 λ3770. We note that the signal-to-noise ratio in this region of the spectrum is rather poor (see Fig. 1) and so the error on T_e(BJ) is quite large. Also, scattered starlight affects the measured magnitude of the Balmer jump. However, by comparison of the flux of the scattered C IV λ5800 emission present in the nebular spectrum (Fig. 1) with the equivalent width of the stellar C IV λ5800 line, we estimate that scattered starlight accounts for only approximately 12 per cent of the observed continuum, and so its effect is small.

Table 6. Empirical ionic abundances of heavy elements derived from CELs.

X^{i+}/H^+	Lines	N_{Xi+}/N_{H+}
N^+	[N II] $\lambda\lambda$6548, 6584	1.30(−6)
O^+	[O II] $\lambda\lambda$3726, 3729	6.37(−6)
O^{2+}	[O III] $\lambda\lambda$4959, 5007	2.96(−4)
Ne^{2+}	[Ne III]$\lambda\lambda$3868, 3967	6.59(−5)
S^+	[S II] $\lambda\lambda$6716, 6731	7.85(−8)
S^{2+}	[S III] λ6312	2.22(−6)
Cl^{2+}	[Cl III] $\lambda\lambda$5517, 5537	7.00(−8)
Cl^{3+}	[Cl IV] $\lambda\lambda$7531, 8046	4.20(−8)
Ar^{2+}	[Ar III] $\lambda\lambda$7135, 7751	9.47(−7)
Ar^{3+}	[Ar IV] $\lambda\lambda$4711, 4740	3.09(−7)
Fe^{2+}	[Fe III] λ4658	3.82(−8)

We also use the weak temperature dependence of some He I line ratios to derive T_e. Table 5 shows that the He I line ratios yield much lower temperatures (4.1–5.1 kK) than those derived from the CEL diagnostics (11.1–15.2 kK). The observed relation T_e([O III])> T_e(BJ)> T_e(He I) is what would be expected in the presence of hydrogen-deficient inclusions within the nebula (Liu et al. 2001b).

3.5.1 Collisionally excited lines

The ionic abundances derived from optical CELs are listed in Table 6. They were derived using a constant temperature of 11.1 kK and a density of 1000 cm^{-3}. As discussed in Section 3.5, recombination excitation may contribute significantly to the flux in the [O II] λ3727,3729 lines, and so the O^+/H^+ abundance derived from them should be considered an upper limit. As the fraction of O in the form of O^+ is very small ($\leqslant$2 per cent), the error this introduces into the total oxygen abundance determination is negligible.

3.5.2 Optical recombination lines

The ionic abundances derived from the measured ORL spectrum of NGC 1501 are listed in Table 7. The ORL abundances were derived using the mean of the measured He I temperature of 5.1 kK, which is expected to be more representative of the temperature in the cold knots that give rise to most of the ORL flux rather than the [O III] temperature or the BJ temperature. The weak dependence of ORL abundances on physical conditions means that the difference between abundances derived adopting the three temperatures are not large.

The He^+/H^+ abundance was derived from the intensities of the λ4471, λ5876 and λ6678 He I lines, weighted 1 : 3 : 1 according to their approximate intensity ratios. According to the formulae given in Kingdon & Ferland (1995), collisional effects are negligible at the temperature of 5.1 kK adopted here. The He^{2+}/H^+ abundance was derived from the He II λ4686 line.

Heavy element ORLs are detected well in our spectrum. Our adopted ORL ionic abundances for C, N and O are the mean of the abundances derived from the selected individual lines for each ion. In Table 7 the ionic abundances that appear between square brackets were left out of the final averages for reasons that will be discussed next. The C II λ5342 line is clearly too strong and must be contaminated by a blend. For this reason, this line is not listed in Table 7. The V3 C II λ7231 line is a component of a 3p–3d transition,

Table 7. Empirical ionic abundances for NGC 1501 from ORLs. The abundances listed between square brackets were not used in the calculation of the averages. See the text for discussion.

Ion	λ (Å)	Mult	trans	I	N_{Xi+}/N_{H+}
He^+	4471.50	V14		3.758	7.29(−2)
	5876.66	V11		11.398	7.32(−2)
	6678.16	V46		3.215	7.22(−2)
	Average				7.29(−2)
He^{2+}	4685.68	3.4		40.299	3.03(−2)
He/H					1.03(−1)
C^{2+}	4267.15	V6	3d–4f	0.987	8.25(−4)
	7231.32	V3	3p–3d	0.131	[3.02(−4)]
	Adopted				8.25(−4)
C^{3+}	4186.90	V18	4f–5g	0.276	2.56(−3)
	4651.47	V1	3s–3p	1.462	[7.00(−3)]
	Adopted				2.56(−3)
C^{3+}	4658.30		5–6	0.100	1.36(−4)
N^{2+}	4035.08	V39a		0.192	1.83(−3)
	4621.39	V5		0.100	3.29(−3)
	5666.63	V3		0.124	1.02(−3)
	5676.02	V3		0.154	2.85(−3)
	Average				2.25(−3)
O^{2+}	3882.29	V11,V12	3p–3d	0.369	[8.90(−3)]
	4285.69	V78b	3d–4f	0.186	7.75(−3)
	4307.23	V53b	3d–4f	0.151	1.14(−2)
	4357.25	V63a	3d–4f	0.108	[1.48(−2)]
	4477.90	V88	3d–4f	0.114	1.05(−2)
	4610.20	V92c	3d–4f	0.133	7.75(−3)
	4661.63	V1	3s–3p	0.451	[3.52(−3)]
	4696.35	V1	3s–3p	0.138	[1.16(−2)]
	Average				9.35(−3)
Ne^{2+}	3777.14	V1		0.278	2.20(−3)
	4397.99	V57b		0.109	[3.26(−3)]
	4409.30	V55e		0.113	[1.76(−3)]
	4413.22	V65		0.157	[6.80(−3)]
	4430.94	V61a		0.136	[4.98(−3)]
	4457.05	V61d		0.124	[1.30(−3)]
	Average				2.20(−3)
Mg^{2+}	4481.21	V4		0.064	6.67(−5)

less reliable than the 3d–4f C II λ4267 transition, and is therefore excluded from the average. For C^{3+} we have preferred to use only the abundance derived from the V18 line at 4186.90 Å, as this is a 4f–5g transition, hence more reliable than the V1 line at 4651.47 Å, which is a 3s–3p transition. Only one C IV line is detected in our spectrum and this is blended with [Fe III] λ4658; we attributed 45 per cent of the total emission to the C IV 5–6 transition (see the discussion in Section 3.7), obtaining $C^{4+}/H^+ = 1.36 \times 10^{-4}$ by number. For O^{2+} only the abundances derived from 3d–4f transitions were finally used for the average, with the exception of the V63a component at 4357.25 Å, which gives a high O^{2+} abundance and may be affected by blending (Tsamis et al. 2004, found that this line is 2.7 times too strong in the spectrum of NGC 3242). In the case of Ne^{2+}, as previously noted by Liu et al. (2000), the 3d–4f coefficients are derived assuming the fine-structure levels of the ground term $2p^4$ $^3P_{2,1,0}$ of Ne^{2+} to be thermalized. However, given that the mean N_e derived for NGC 1501 is more than an order of magnitude lower than the critical densities of the $^3P_1$ (2.0×10^5 cm^{-3}) and the $^3P_0$ (2.9×10^4 cm^{-3}) levels of Ne^{2+}, the assumption of Boltzmann equilibrium is probably unrealistic. At the lower densities of NGC 1501 we expect the $^3P_1$ and $^3P_0$ levels to be underpopulated and the $^3P_2$ level to be overpopulated. As the strongest 3d–4f lines originate from the $^3P_2$ level, their recombination coefficient would be underestimated leading to correspondingly overestimated abundances. From our observations the mean abundance derived from 3d–4f transitions is a factor of 1.7 higher than the abundance yielded by the 3s–3p V1 multiplet. In the light of the above discussion we adopt the Ne^{2+}/H^+ abundance derived from Ne II multiplet VI only.

3.6 Summary of nebular empirical abundances

Total elemental abundances were first of all derived using the ionization correction factor scheme of (Kingsburgh & Barlow 1994, KB94) (see columns 2 and 4 of Table 8). For oxygen, O^+/H^+ and O^{2+}/H^+ abundances are available from CELs, and the unseen O^{3+} was corrected for using

$$\frac{O}{H} = \left(\frac{He^+ + He^{2+}}{He^+}\right)^{2/3} \left(\frac{O^+ + O^{2+}}{H^+}\right). \quad (1)$$

The ionization correction factor derived from this is 1.27. For oxygen ORLs, only O^{2+}/H^+ is available, and to derive a total abundance it was assumed that the ORL O^+/O^{2+} ratio was the same as the value of 0.022 derived from CELs, giving an ionization correction factor (ICF) of 1.30. It is worth noting at this point that the ionic fractions in the ORL- and CEL-emitting regions may actually differ, but, while we cannot constrain the exact amount, we expect that only a small fraction of oxygen to be in the form of O^+, even in the coldest regions (e.g. Ercolano et al. 2003b), and so the errors in the determination of O/H should be small.

The nitrogen abundance from CELs is rather uncertain – only [N II] lines are seen, and N^+ accounts for only a small fraction of the total nitrogen abundance. KB94 give $N/H = (N^+/H^+)(O/O^+)$, which gives an ionization correction factor of 60.39. Uncertainties of the empirical determination of the ICF for N are discussed toward the end of this section. In the case of the ORLs, N^{2+} and N^{3+} abundances are available. The unseen N^+ is corrected for by assuming that $N/N^+ = O/O^+$, which results in an ionization correction factor of 1.02.

No carbon CELs are seen as only optical nebular spectra were available. As discussed in Section 2.2, the *IUE* observations of this object are unsuitable for nebular analysis. However, nebular C II, C III and C IV ORLs are seen in our optical spectra, and a total carbon ORL abundance of 3.52×10^{-3} by number with respect to hydrogen is derived.

One magnesium line is seen in our spectrum – that of Mg II λ4481. No ionization correction scheme exists for magnesium, but Mg^{2+}

Table 8. ICFs and total elemental abundances by number with respect to H derived from CELs and ORLs.

Ion	ICF		Abundance	
	KB94	MC2	KB94	MC2
	From CELs			
N	60.4	252	7.85(−5)	3.28(−4)
O	1.27	1.13	3.85(−4)	3.42(−4)
Ne	1.30	1.06	8.57(−5)	6.98(−5)
S	2.73	14.4	6.29(−6)	3.31(−5)
Cl	2.83	1.13	1.98(−7)	1.27(−7)
Ar	1.02	1.03	1.28(−6)	1.29(−6)
Fe	–	155	–	5.92(−6)
	From ORLs			
C	1.02		3.52(−3)	
N	1.02		2.29(−3)	
O	1.30		1.22(−2)	
Ne	1.30		2.86(−3)	

occupies a very large ionization potential interval, from ∼15 to ∼80 eV, and so almost all the magnesium present will be in the form of Mg^{2+}. The abundance derived for Mg^{2+} is noteworthy. While all the second-row elements have ORL abundances that are much higher than those derived from CELs and exceed the solar abundance by factors of 10–30, the abundance derived for magnesium, using the ICF of the model MC2 (see Table 8 and Sections 4 and 5), is only a factor of 1.9 higher than the solar value. This is in line with the Mg abundances found by Barlow et al. (2003) for other nebulae showing large CNO ORL/CEL discrepancies, and strongly suggests that the large CNO ORL abundances are due to astrophysical effects such as H-deficient knots, and not to some unknown atomic process, as the latter might be expected to affect third- and second-row elements.

Argon, sulphur and chlorine abundances are derived from CELs only (see Table 6), with KB94 ionization correction factors of 1.02, 2.73 and 2.83, respectively.

The [Fe III] λ4658 line is contaminated by the C IV λ4658 line (see Table 1). However, from the measured intensity of [Fe III] λ4881 (Table 1), the second strongest line in the optical spectrum of [Fe III], and the theoretical [Fe III] λ4658/λ 4881 intensity ratio of 2.0 at $T_e = 12$ kK and $N_e = 10^3$ cm^{-3} (collision strength and A-value from Zhang 1996; Nahar 1996, respectively), we estimate that [Fe III] contributes 55 per cent to the 4658-Å blend, with C IV contributing the rest. This yields $Fe^{2+}/H^+ = 3.82 \times 10^{-8}$ (see Table 6). Using an ICF of 155 from the model MC2, we derive a CEL-based total Fe abundance of 5.92×10^{-6}, by number with respect to hydrogen.

We also calculated total abundances from the CELs using the ICFs from model MC2. Columns 3 and 5, in the upper half of Table 8, list the model ICFs and corresponding total abundances, obtained by applying the ICFs to the ionic abundances derived from the CEL analysis. Total elemental abundances obtained using the MC2 ICFs should be more accurate than those obtained by using the KB94 ICFs and are adopted in this work. The largest discrepancy between the KB94 ICFs and the model ones is found for nitrogen. The CEL ionic abundances, together with the KB94 ICFs, give N/O = 0.20, which would make NGC 1501 a non-Type I PN according to both the criterion of (Peimbert & Torres-Peimbert 1983 N/O > 0.5 for a Type I PN) and the criterion of KB94 (N/O > 0.85 for a Milky Way Type I PN). However, the factor of 4 difference between the KB94 and MC2 ICFs for nitrogen turns NGC 1501 into a Type I PN when using the MC2 ICFs, with $(N/O)_{CEL} = 0.96$.

For the ORLs, when using MC2 ICFs we find N/O = 0.52, while for the KB94 ICFs we find N/O = 0.19. However, as CEL abundances are believed to provide a better representation of 'average' nebular gas (see, e.g., Péquignot et al. 2003), the classification of NGC 1501 as a Type I PN is preferred here. The elemental abundances derived from the CELs using MC2 ICFs are listed in Table 9, where they are compared with the ORL-based abundances, with average local disc PN abundances from KB94, and with solar abundances. For N, O and Ne, the ORL-based abundances are larger than the CEL-based abundances by factors of 7, 36 and 42, respectively.

Table 9. Recommended elemental abundances in NGC 1501 from CELs and ORLs, in units such that $\log N(H) = 12.0$.

Element	ORLs	CELs	PN[a] Average	Solar[b]
He	11.01	–	11.06	10.93
C	9.55	–	8.74	8.39
N	9.36	8.52	8.35	7.92
O	10.09	8.53	8.68	8.69
Ne	9.46	7.84	8.09	8.08
S	–	7.52	6.92	7.33
Cl	–	5.10	–	5.50
Ar	–	6.11	6.39	6.40
Fe	–	6.77	–	7.52

[a]The overall average abundances of Galactic PNe (Kingsburgh & Barlow 1994);
[b]Solar abundances from Grevesse & Sauval (1998, 1999), apart from C and O abundances, which are from Allende Prieto, Lambert & Asplund (2001, 2002).

4 THREE-DIMENSIONAL PHOTOIONIZATION MODELLING OF THE NEBULA

4.1 The computer code and model setup

The three-dimensional photoionization code MOCASSIN, Version 1.10 (Ercolano et al. 2003a) was used in order to construct a realistic model for NGC 1501. Sets of models were run, of which we selected two, MC1 and MC2, which best reproduced the nebular emission spectrum. The initial models (MC1) were run on the HIPERSPACE facilities at University College London, consisting of a SUN Microsystems V880 multiprocessor computer with 16 processors and 32 Gb of memory. The later models (MC2) were run on a Beowulf cluster that belongs to the Institute of Computational Mathematics and Scientific/Engineering Computing of the Chinese Academy of Sciences, consisting of 120 550-MHz Pentium III processors with 1 Gb of memory each. A grid of 71^3 spatial points was used for our final models, corresponding to 357 911 cubic cells of length 1405 au each (assuming a distance of 1300 pc). The only difference between the MC1 and MC2 models is that the latter uses test values (see Section 5.1.1) for the unknown low-temperature dielectronic recombination coefficients of third-row elements (S, Cl and Ar), while the former sets all unavailable rates to zero. The nebular and stellar input parameters, as well as the final model abundances for MC1 and MC2, are listed in Table 10.

4.2 The density distribution

The three-dimensional density distribution grid used for the modelling was determined for by Ragazzoni et al. (2001) from long-slit echellograms, reduced according to the methodology developed by Sabbadin et al. (2000a,b). As the density distribution is, in

Table 10. Input parameters for the MOCASSIN photoionization models. The abundances listed in this table are the final abundances used in models MC1 and MC2.

Stellar and nebular parameters			Nebular abundances Model	CEL
T_{eff} (kK)	110	He/H	0.110	–
log g (cgs)	6.0	C/H	3.40(−4)	–
L_* ($L_\odot$)	5000	N/H	3.16(−4)	3.28(−4)
D (kpc)	1.3	O/H	3.50(−4)	3.42(−4)
ϵ	0.423	Ne/H	6.35(−5)	6.98(−5)
R_{cube} (arcsec)	38	Mg/H	3.80(−5)	–
		Si/H	1.00(−5)	–
		S/H	3.10(−5)	3.31(−5)
		Cl/H	1.20(−7)	1.27(−7)
		Ar/H	1.10(−6)	1.29(−6)
		Fe/H	6.60(−6)	5.92(−6)

general, a difficult input parameter to constrain, given the plurality of acceptable solutions, the existence, in this case, of a model density directly derived from the observations puts us in a favourable position, allowing a potentially higher degree of accuracy in the determination of the other nebular and central star parameters. The data cube made available to us by F. Sabbadin consisted of a 200^3 grid of N_e; these were mapped to the 71^3 MOCASSIN grid and converted to gas densities by iteratively using the local ionization structure calculated at each grid cell to calculate the conversion factors.

Figs 4 and 5 of Ragazzoni et al. (2001) show iso-density plots of the N_e distribution they derived at two different threshold values ($N_e = 300$ cm^{-3} and $N_e = 900$ cm^{-3}), as seen from 12 different directions, while the optical appearance of the rebuilt nebula as seen from the same 12 directions is shown in their fig. 6. It is worth noting at this point that the original N_e cube contained values of $N_e(\mathrm{H}\alpha)$, where $N_e(\mathrm{H}\alpha) = N_e(\mathrm{S\,II})\,\epsilon^{1/2}$, ϵ being the local filling factor. Unfortunately, the value of ϵ could not be determined from Ragazzoni et al.'s observations. The value of 0.423 used in the MOCASSIN models (and reported in Table 10) was chosen in order to reproduce $I(\mathrm{H}\beta) = 5.26 \times 10^{-11}$ erg s^{-1} cm^{-2}, the integrated H(β) flux from Cahn et al. (1992), dereddened using $c(\mathrm{H}\beta) = 1.0$ (see Section 3.3). This was made possible by the fact that this large, old, low-electron density PN is optically thin in H I, implying that the Hβ emission of the nebula is not dependent on the luminosity of the central star, but represents a measure of the ionized mass. From this it is clear that $I(\mathrm{H}\alpha) \propto N^2{}_e\epsilon/D^2$, where D is the distance from the nebula. As is true for many astronomical objects, the distance to NGC 1501 is quite poorly constrained. At least 15 estimates are available in the literature, including statistical and individual distance estimates, with values ranging from 0.9 (Amnuel et al. 1984) to 2.0 kpc (Acker 1978). The value of 1.30 kpc adopted in this work, was chosen for reasons of consistency with the value adopted by Ragazzoni et al. (2001) for their calculation of the three-dimensional ionization structure from observations. We finally note that, although S^+ may not be a faithful representation of the ionized gas in this high-excitation nebula, Ragazzoni et al.'s result is certainly an improvement from the assumption of a spherically symmetric analytical density law.

4.3 Elemental abundances

A homogeneous elemental abundance distribution was used for our models given that, although the ORL–CEL ADFs are high in this nebula, which may indicate the presence of cold ionized hydrogen-deficient material (e.g. Liu et al. 2000), we do not have any direct observational evidence for the presence of structures containing plasma with different elemental abundances. It is, however, possible that such structures might exist inside the nebular shell, but with sizes falling below the spatial resolution of the instruments currently available. With the *HST*, a spatial resolution of 0.045 arcsec can be achieved in the optical – this corresponds to 53 au at 1300 pc. *HST*/WFPC2 images of NGC 1501 have been taken as part of the GO program 6119. However, the observations were aimed at detecting companions to central stars, and the short exposures necessary to obtain good stellar images yield very poor signal-to-noise ratios for the nebula itself. Also, the observations were taken in broad-band filters F555W and F814W, which contain many emission lines and are thus impossible to use for quantitative nebular analysis. As will be discussed in more detail in Section 6, the presence of small, hydrogen-deficient knots could provide an explanation for the aforementioned ORL–CEL discrepancies and other spectroscopic peculiarities.

The abundances derived empirically from CELs (see Section 3.5) were used as starting values for our modelling; these were then modified in order to obtain a better fit to the CEL spectrum.

4.4 Central star parameters

The effective temperature and gravity of the central star were varied in order to provide an ionizing spectrum that could reproduce the ionization structure implied by the observed nebular spectrum, under the constraints of our adopted density distribution, filling factor and distance. The final values adopted are $T_{\mathrm{eff}} = 110$ kK and $\log g = 6.0$ (cgs). This is well within the range of effective temperature determinations available in the literature, which range from $T_{\mathrm{Zanstra}}(\mathrm{He\,II}) = 81$ kK (Stanghellini et al. 1994) to the value of 135 kK obtained by Koesterke & Hamann (1997) by means of stellar atmosphere modelling. It is worth noting at this point that, within a certain range of gravities, the value of $\log g$ has a negligible influence on the ionizing flux level of these models.

The hydrogen-deficient non-LTE stellar atmospheres used in this work were calculated using the Tübingen NLTE Model Atmosphere Package (Rauch 2003), for He : C : N : O = 33 : 50 : 2 : 15 by mass, i.e. abundances close to those derived for the central star of NGC 1501 and for PG 1159 stars (see Section 3.4). These models are available for download from Dr T. Rauch's website (http://astro.uni-tuebingen.de/~rauch). The best results for the nebular photoionization modelling were obtained with a central star effective temperature of 110 kK (as mentioned above) and a stellar luminosity of $L_* = 5000\,\mathrm{L}_\odot$, which is close to the 5500-$\mathrm{L}_\odot$ estimate of Koesterke & Hamann (1997). This model was found to be consistent with the level of the stellar UV continuum between 1300–1800 Å in the dereddened *IUE* spectrum (see Section 2.2).

4.5 The ionizing spectrum

As discussed in Section 3.2, evidence for a strong stellar wind is observed in the spectrum of the central star of NGC 1501. This poses the question of whether a model atmosphere calculated with the plane parallel Tübingen code is a justifiable choice. We compared it with a model atmosphere calculated with the spherically symmetric code CMFGEN (Hillier & Miller 1998), for wind parameters close to those of the central star of NGC 1501 and abundances He : C : N : O = 54 : 36 : 1 : 8 by mass, similar to those derived by (Koesterke & Hamann 1997 He : C : O = 50 : 35 : 15), with a Tübingen model for the PG 1159-type abundances given above; both models had $T_{\mathrm{eff}} = 135$ kK. Despite the different abundances, the variations in the flux levels between the two models were found to be less than a factor of 2, for wavelengths shortward of the Lyman limit, which is within the error bars imposed by the uncertainties of the stellar abundance determination. We also compared our Tübingen model atmosphere at 110 kK with one calculated by L. Koesteke (private communication) using a spherically symmetric wind model for the same temperature and PG 1159-type abundances, and found that the flux levels predicted by the two models agreed to within 20 per cent.

5 NEBULAR MODELLING: STRATEGY AND RESULTS

The results of our photoionization modelling and a comparison with observed values are presented in this section. Our preliminary modelling was aimed at constraining the basic stellar and nebular parameters. Bearing in mind that the empirical analysis of the ORL

Table 11. Collisionally excited emission-line intensities predicted by MOCASSIN, compared with observed values. The line intensities are given relative to $I(\mathrm{H}\beta)$ on a scale where $I(\mathrm{H}\beta) = 100$. The intensity of Hβ is given in absolute units (erg cm^{-2} s^{-1}) and is compared with the value given by (Cahn et al. 1992), dereddened by $c(\mathrm{H}\beta) = 1.0$.

Line	MC1	MC2	Observed
Log[$I(\mathrm{H}\beta)$]	−10.27	−10.27	−10.28
Hβ λ4861	100	100	100
[N II] λ5755	0.20	0.20	0.25
[N II] λ6548	3.44	3.45	3.16
[N II] λ6584	10.14	10.01	9.94
[O II] λ3727	5.44	10.7	12.16
[O II] λ3729	4.69	9.23	10.08
[O II] λλ7318,9	0.21	0.41	0.73
[O II] λλ7330,0	0.17	0.33	0.59
[O III] λ4363	12.81	12.78	10.38
[O III] λ4932	0.19	0.19	0.35
[O III] λ4959	458	456	394
[O III] λ5007	1319	1312	1151
[Ne III] λ3869	102	103	101
[Ne III] λ3967	31.6	31.7	28.10
[S II] λ4069	0.069	0.28	1.49
[S II] λ4076	0.023	0.10	0.32
[S II] λ6717	0.43	1.76	1.77
[S II] λ6731	0.48	1.98	1.95
[S III] λ 6312*	1.48	1.48	1.48
[Cl III] λ5518	0.11	0.84	0.76
[Cl III] λ5538	0.090	0.71	0.72
[Cl IV] λ7531	0.56	0.26	0.26
[Cl IV] λ8046	1.31	0.61	0.54
[Ar III] λ7136	1.30	13.08	14.34
[Ar III] λ7752	0.31	3.16	3.52
[Ar IV] λ4712	9.02	2.74	2.66
[Ar IV] λ4741	7.01	2.12	2.00

*Blend with He II λ6310.

spectrum of NGC 1501 yields larger abundances than the CEL analysis, and that this could be interpreted as indicating the existence of a separate component in the nebular gas, our efforts aimed to match the CEL spectrum only, as this should be representative of the dominant mass component of the nebular gas (Liu et al. 2000; Péquignot et al. 2003).

5.1 The first model (MC1)

The initial model will be referred to in this paper as MC1. The CEL intensities predicted by MC1 are compared with the observed values in Table 11. Table 12 lists the predicted and observed nebular diagnostic line ratios. The results obtained from this first round of modelling, of which only the best-fitting model is shown in the table, were quite surprising. A comparison of the CEL intensities predicted by the model with the observations indicates that the model is too highly ionized. However, this is at odds with what is implied by the predicted He I and He II recombination lines, which show that the degree of ionization of He is actually slightly lower than indicated by observations (see Table 13). The problem is evident from examination of the values listed in Table 14, containing the X^{i+1}/X^{+i} model ionic fractions (columns 2 and 3) and those derived from the empirical analysis (column 4). Changes of the central star ionizing spectrum, aimed to adjust the ionization degree of O, S, Cl and Ar

Table 12. Calculated and observed plasma diagnostic ratios.

Ion	Lines	IP (eV)	Observed	MC1	MC2
[S II]	$I(\lambda6731)/I(\lambda6716)$	10.36	1.10	1.12	1.12
[O II]	$I(\lambda3729)/I(\lambda3726)$	13.62	0.83	0.86	0.86
[O II]	$I(\lambda3727)/I(\lambda7325)$	13.62	16.85	26.84	26.11
[Cl III]	$I(\lambda5537)/I(\lambda5517)$	23.81	0.95	0.84	0.84
[Ar IV]	$I(\lambda4740)/I(\lambda4711)$	40.74	0.75	0.78	0.77
[N II]	$I(\lambda6548+\lambda6584)/I(\lambda5754)$	14.53	52.38	68.67	68.60
[O III]	$I(\lambda4959+\lambda5007)/I(\lambda4363)$	35.12	148.7	138.7	138.4
He I	$I(\lambda5876)/I(\lambda4471)$	24.59	3.03	2.72	2.72
He I	$I(\lambda6678)/I(\lambda4471)$	24.59	0.86	0.76	0.76

Table 13. Helium recombination line intensities predicted by MOCASSIN, compared with observed values. The line intensities are given relative to $I(\mathrm{H}\beta)$ on a scale where $I(\mathrm{H}\beta) = 100$. The intensity of Hβ is given in absolute units (erg cm^{-2} s^{-1}) and is compared with the value given by (Cahn et al. 1992), dereddened by $c(\mathrm{H}\beta) = 1.0$.

Line	MC1	MC2	Observed
Log[I(Hβ)]	−10.27	−10.27	−10.28
Hβ λ4861	100	100	100
He I λ4471	4.20	4.20	3.76
He I λ4922	1.11	1.11	1.07
He I λ5876	11.42	11.43	11.40
He I λ6678	3.21	3.21	3.12
He I λ7065	2.16	2.16	2.51
He II λ4686	34.7	34.6	40.30

Table 14. Predicted and observed ionic ratios.

X^{i+1}/X^{i}	MC1	MC2	obs	MC1/obs	MC2/obs
O^{2+}/O^{+}	116	58.9	46.5	2.49	1.27
S^{2+}/S^{+}	46.8	27.8	28.3	1.65	0.98
Cl^{3+}/Cl^{2+}	10.4	0.61	0.60	17.4	1.02
Ar^{3+}/Ar^{2+}	12.0	0.35	0.33	36.2	1.06
X^{i+1}/X^{i}	MC1	MC2	obs	MC1/obs	MC2/obs
He^{2+}/He^{+}	0.36	0.36	0.41	0.88	0.88

in the nebula, would necessarily also affect the ionization structure of He, thus causing a larger discrepancy with the observations. This was confirmed by a comparison of models run with several $T_{\rm eff}$ − log g combinations within the range $T_{\rm eff} = 100$–140 kK and log $g =$ 5.0 –8.0 (cgs).

5.1.1 The problem of data incompleteness for the low-temperature dielectronic recombination process

The overionization problem of S, Cl and Ar could be interpreted as evidence for the effects of low-temperature dielectronic recombination, a process that can in magnitude be comparable (or often larger) than its radiative counterpart, but for which no reliable rates have yet been calculated for third-row elements. The uncertainty of the atomic data available for some astrophysically abundant elements is faced by all photoionization codes. Ali et al. (1991) argued that, for a given ion X^{+i}, a better estimate than zero is obtained by taking the average of the rate coefficients for C^{+i}, O^{+i} and N^{+i}, given that

the coefficients seem to follow a certain trend with ionization stage. Dudziak et al. (2000), use coefficients empirically calibrated from a new unpublished model of the PN NGC 7027. In this work, we do not attempt to calculate empirical coefficients, as NGC 1501, with its complicated nebular spectrum and WR central star, cannot be considered a typical PN. Self-consistent calculations of dielectronic and radiative rates of some third-row elements are currently being carried out (Storey, Ercolano & Badnell, in preparation), but in this paper we will limit ourselves to seeking empirical upper limits to the unknown dielectronic rates and use these coefficients as test values for our nebular modelling.

For a pocket of gas in ionization equilibrium, the abundance ratio of two successive ionic stages is given by

$$\frac{X^{i+1}}{X^i} \sim \frac{N_{\rm phot}^{X^{+\rm i}}}{N_{\rm e}\left[\alpha_{\rm R}(X^{+\rm i}, T_{\rm e}) + \alpha_{\rm D}(X^{+\rm i}, T_{\rm e})\right]}, \quad (2)$$

where $N_{X^{+\rm i}}^{\rm phot}$ is the total number of photoionization events and $\alpha_{\rm R}(X^{+\rm i}, T_{\rm e})$ and $\alpha_{\rm D}(X^{+i}, T_{\rm e})$ are the temperature-dependent rate coefficients for, respectively, radiative and dielectronic recombination to X^{+i}. Note that we are assuming that the contribution due to charge exchange processes is negligible in this case, given that the nebula is optically thin in H I. This implies that we can use the ratio of model to observed X^{i+1}/X^i values to obtain an estimate of $\alpha_{\rm D}(X^{+i}, T_{\rm e})$:

$$\alpha_{\rm D}(X^{+i}, T_{\rm e}) = \left[\frac{(X^{i+1}/X^{+i})^{\rm mod}}{(X^{i+1}/X^{+i})^{\rm obs}} - 1\right] \alpha_{\rm R}\left(X^{+i}, T_{\rm e}\right). \quad (3)$$

Unfortunately, our observations did not yield all the X^{i+1}/X^{+i} ratios necessary to derive a consistent set of estimates for all the relevant ionic stages of S, Cl and Ar, but only for S^+, Ar^{2+} and Cl^{2+}. We define a quantity $f(X^{+i})$ such that the dielectronic rates for each ionic stage can be expressed as $\alpha_{\rm D}(X^{+i}, 10^4\ {\rm K}) = f(X^{+i})\,\alpha_{\rm R}(X^{+i}, 10^4\ {\rm K})$, where initial guesses for $f(X^{+i})$ were taken from equation (3) and then adjusted iteratively with the modelling. From the above, $f(X^{+i})$ is defined as the ratio of the low-temperature dielectronic recombination coefficient to the radiative recombination coefficient of the ion $X^{\rm i}$ at $T_{\rm e} = 10^4$ K. The use of a temperature independent coefficient such as $f(X^{+i})$ is equivalent to saying that the dielectronic rates follow the same temperature dependence as the radiative rates for the same ion, which is, of course, not true. Nevertheless, this is the best we can do in this case, as we are not attempting to calculate precise rates, a task that can only be fulfilled by laboratory measurements or detailed atomic modelling of each individual ion. Furthermore, the nebular gas $T_{\rm e}$s do not show large deviations from a mean of 11 100 K, and therefore the error introduced by the temperature dependence will be much smaller than the margin of error implied by our empirical approach. The final $f(X^{+i})$ values used are given in Table 15, together with the corresponding values of $\alpha_{\rm D}(X^{+i}, T_{\rm e})$ for $T_{\rm e} = 10^4$ K. These values are only to be considered as upper limits, as other effects may be at play in complicating the ionization structure of this object (see Section 6). As a comparison, the low-temperature dielectronic recombination coefficients and the corresponding f values are listed in Table 16 for C, N and O ions (Nussbaumer & Storey 1984) at 10 kK. Using the Ali et al. (1991) method described above with the values listed in Table 16, one obtains estimates of 3.25×10^{-12} and 1.55×10^{-11} cm^3 s^{-1} for the singly- and doubly ionized cases at $T_{\rm e} = 10$ kK, lower than the values listed in Table 15, necessary to resolve the discrepancy with the observations.

Table 15. Estimated upper limits to low-temperature dielectronic rates.

X^i	$f(X^i)^a$	$\alpha_{\rm D}(X^i, 10^4 K)$ (cm^3 s^{-1})
S^+	3.14	5.66(−12)
Cl^{2+}	17.5	5.81(−11)
Ar^{2+}	42.5	13.7(−11)

[a] $f(X^i) = \alpha_{\rm D}(X^i, 10^4\ {\rm K})/\alpha_{\rm R}(X^i, 10^4\ {\rm K})$.

Table 16. Low-temperature dielectronic rates for CNO ions (Nussbaumer & Storey 1984).

X^i	$f(X^i)^a$	$\alpha_{\rm D}(X^i, 10^4$ K) (cm^3 s^{-1})
C^+	2.4	6.06(−12)
C^{2+}	2.7	1.36(−11)
N^+	0.86	2.03(−12)
N^{2+}	4.1	2.16(−11)
O^+	0.83	1.66(−12)
O^{2+}	2.0	1.14(−11)

[a] $f(X^i) = \alpha_{\rm D}(X^i, 10^4\ {\rm K})/\alpha_{\rm R}(X^i, 10^4\ {\rm K})$

5.2 Models including estimated low-temperature dielectronic recombination rates for third-row elements (MC2)

5.2.1 The CEL spectrum

The CEL intensities predicted by the best-fitting model from a second set of models (MC2), which use the estimated upper limits to the dielectronic recombination rates given in Table 15, are given in column 3 of Table 11. This model provides a much better fit to the overall observed emission-line spectrum than model MC1, but some problems are still present, as discussed in Section 6.

The ionization degree of O also appeared to be overestimated by model MC1 (see Table 14). The dielectronic rates included in the atomic data base of MOCASSIN, were obtained by Nussbaumer & Storey (1984) who performed the calculations within the LS coupling scheme. As discussed in Section 4.3 of the Nussbaumer & Storey (1984) paper, using intermediate coupling (IC; e.g. Beigman & Chichkov 1980) could result in higher rates as more states are taken into account (although not all of these would be permitted to autoionize). With this in mind, we increased the dielectronic rates in MC2 by a factor of 3, which returned a better fit of the oxygen CEL spectrum. However, as discussed in Section 6, the large corrections to the atomic data required by MC2 are questionable and highlight the limitations of this chemically homogeneous model.

The [O II] λ7319 and λ7330 doublets and the [S II] λ4069 and λ4076 lines are still underestimated by model MC2. Recombination processes can contribute to the intensity of these lines, and, whilst effective recombination coefficients to the metastable levels of [O II] are known (Liu et al. 2000), the same is not true for [S II]. We have included the recombination term to the statistical equilibrium matrix in our photoionization model, in order to self-consistently calculate the populations of the metastable levels of [O II], by taking into account recombination and collisional population and depopulation. However, at the temperatures and densities of the nebular gas, we found recombination contributions to be negligible. We therefore conclude that the discrepancy between model and observed intensities of these line must be attributed to recombination processes occurring in a separate, colder and/or denser gas phase (see Section 6).

Table 17. Nebular-averaged fractional ionic abundances, obtained from model MC2.

Element	Ion I	II	III	IV	V	VI	VII
H	1.27(−3)	9.99(−1)					
He	7.43(−4)	7.34(−1)	2.65(−1)				
C	4.60(−6)	8.89(−3)	4.09(−1)	5.67(−1)	1.49(−2)		
N	9.95(−7)	3.97(−3)	3.91(−1)	6.02(−1)	3.11(−3)		
O	1.24(−5)	1.47(−2)	8.66(−1)	1.18(−1)	1.31(−3)		
Ne	9.37(−7)	5.03(−3)	9.42(−1)	5.30(−2)	3.36(−5)		
Mg	2.98(−3)	3.11(−2)	9.15(−1)	5.12(−2)	1.93(−6)		
Si	5.40(−5)	3.77(−2)	2.64(−1)	4.18(−1)	2.80(−1)		
S	3.36(−7)	2.42(−3)	6.72(−2)	4.87(−1)	4.39(−1)	4.41(−3)	5.89(−6)
Cl	1.13(−6)	4.44(−3)	5.51(−1)	3.57(−1)	1.05(−1)	2.94(−3)	1.12(−7)
Ar	1.18(−7)	9.40(−4)	7.14(−1)	2.53(−1)	2.90(−2)	2.63(−3)	9.37(−6)
Fe	4.05(−5)	6.72(−4)	6.44(−3)	6.47(−1)	3.13(−1)	3.22(−2)	2.15(−5)

5.2.2 The computed ionic and thermal structure of the nebula

The nebular-averaged fractional ionic abundances calculated from the MC2 model are listed in Table 17. Hydrogen and helium are both fully ionized and we see that significant fractions of the heavy elements are in higher ionization stages. We note that the N/N^+ ratio is nearly a factor of 3 larger than the O/O^+ ratio, contrary to what is generally assumed in ionization correction schemes, including that used in this work, where the two ionic fractions are taken to be the same. This has already been noted by Rubin et al. (1988) and should be taken into account when considering uncertainties in empirical abundance analyses for optically thin PNe such as NGC 1501 (see also Section 3.7).

We did not find large temperature fluctuations in the computed three-dimensional temperature distribution, obtaining $t^2(O^{2+}) = 0.0021$ from the model. This is not surprising, given that large density fluctuations are not present in our density distribution grid.

6 THE USUAL SUSPECTS: t^2 VERSUS ENHANCED-DENSITY, METAL-RICH KNOTS

The introduction of the test values for the low-temperature dielectronic recombination coefficients of S, Ar and Cl certainly helped to achieve a better fit to the observed CEL spectrum of NGC 1501. However, a number of problems still remain unsolved, in particular the following.

(i) The ORL–CEL discrepancy. MC2 fails to reproduce the observed ORL spectrum. The abundances derived empirically from the ORL spectrum are consistently larger than those derived from the CEL analysis, while the T_e derived from the observed He I recombination lines is cooler than the temperature estimates obtained from CELs (Table 5).

(ii) The large dielectronic rate value for argon. With regards to the Ar^{3+}/Ar^{2+} ionic ratios, large low-temperature dielectronic recombination rates are required in order to resolve the discrepancy between the observations and the photoionization models. Although strongly dependent on the atomic structure of each individual ion, atomic data currently available for a number of doubly ionized ions show low-temperature dielectronic rates to be at most 10 times larger than the corresponding radiative rates (with average values being in the region of 3 or 4 times the radiative rates). On the other hand, recent work by Morisset et al. (2004) also pointed out the need for large dielectronic rates for Ar^{2+} in order to reconcile *ISO* infrared observations and models for 40 H II regions in their sample.

Temperature fluctuations have been proposed within the t^2 framework of Peimbert (1967, 1971, and later references) by (e.g. Ruiz et al. 2003) and Peimbert et al. (2004) as a solution to the ORL–CEL abundance discrepancy. In the case of NGC 1501 our three-dimensional models showed no evidence for t^2 fluctuations larger than 0.012. We also calculated empirical values for T_0([O III]) and t^2([O III]), following the formulations given by Peimbert (1967, 1971) and, more recently Peimbert et al. (2004). First of all we calculated that a value of T_0([O III]) = 3750 K is required to obtain the same abundances from the [O III] CELs and the O II ORLs, implying 43 per cent temperature fluctuations [t^2([O III]) = 0.184]. However, when we derived values for the same quantities using the Balmer jump and the [O III] temperatures from Table 5, we found a mean temperature of T_0([O III]) = 10 010 K and t^2([O III]) = 0.036, which correspond to temperature fluctuations of only 19 per cent. We also calculated T_0 and t^2 values using the T_e derived from the He I recombination lines (see Table 5). The He I λ5876/λ 4471 T_e of 4100 K implies that $T_0 = 5350$ K and $t^2 = 0.154$, while the mean He I T_e of 5125 K implies that $T_0 = 6300$ K and $t^2 = 0.133$. These values of T_0 and t^2 would increase the O^{2+} abundance measured from CELs by factors of 10.6, 3.3 and 6.5, respectively, still a long way short of resolving the factor of 30 discrepancy. The observational results and the computed three-dimensional temperature structure indicate that something other than temperature fluctuations is causing the large ORL–CEL ADFs we found for NGC 1501.

The existence of metal-rich knots could provide a solution to the problems mentioned above. While such knots have been invoked recently to help with the solution of the ORL–CEL discrepancy problem in PNe (e.g. Liu 2002), and bi-abundance photoionization models have been constructed for some PNe (Péquignot et al. 2003), it is further proposed here that the lower ionization degree of heavy elements compared with helium shown by NGC 1501 can also be explained by the presence of small metal-rich knots mixed with the nebular gas. The knots could be formed by processed material transported out in the outflow from the asymptotic giant branch (AGB) precursor of the H-deficient WR central star.

Low-ionization species would be abundant in the knots and in the shadow regions (tails) behind them, thanks to softening of the radiation field due to the screening effect of material that is optically thick to stellar UV radiation. However, due to the high metallicity and cooling rates in the material, the temperatures inside the knots are expected to be much too low for collisionally excited line radiation to be produced to a significant degree, while essentially all the ORL emission is expected to be produced in these regions (see,

e.g., the 3D photoionization model of the H-poor knots in Abell 30 by Ercolano et al. 2003b).

The situation in the shadowed tails of knots is completely different. As these are composed of material with normal nebular abundances, they are not as efficiently cooled as the knots themselves, implying that the emission of collisionally excited lines from lower ionization species would be expected. In this regard it is clear that the problem of overionization of oxygen in the CEL-emitting region for models MC1 and MC2 could be eased by the introduction of such knots, which could also provide some of the missing emission from S^+, Ar^{2+} and Cl^{2+}, with the implication that lower dielectronic rates than those listed in Table 15 would be sufficient to match the CEL spectrum.

7 CONCLUSIONS

In this paper we have presented new, deep optical spectra of the PN NGC 1501. The empirical analysis led to the discovery of high ORL–CEL ADFs for O^{2+} and Ne^{2+}, with values of 32 and 33, respectively. The agreement between the ADFs for O and Ne lends further weight to the suggestion by Liu et al. (2000) that, while large discrepancies may exist between ORL and CEL abundances relative to H, elemental ratios such as Ne/O are often the same whether derived from CELs or ORLs.

Unfortunately, no temperature for the ORL-emitting region could be determined from our observations, as the O II λ4089 line (see Wesson, Liu & Barlow 2003; Tsamis et al. 2004) was not detected in our observations. However, a large temperature discrepancy exists between the T_e implied by the He I recombination line ratios (on average ∼5.1 kK) and the [O III] temperature (11.4 kK). Given that we expect T_e(ORL) < T_e(He I)< T_e(CEL) (Liu 2003), the ORL emitting regions probably have temperatures lower than 4.5 kK, consistent with the results of Wesson et al. (2003) for knot J3 of Abell 30, where T_e(ORL) = 2.5 kK. T_e(He I)> T_e(ORL) is a logical consequence of He I recombination lines being produced in both the ORL and the CEL-emitting regions and, therefore, the T_es derived from them are not representative of either region.

Our initial models showed metals to be too highly ionized compared with observations, except for helium. We suspect that two effects are at play in complicating the emission-line spectrum of NGC 1501. First of all, we note the incompleteness of low-temperature dielectronic recombination coefficients for third-row elements and the possible underestimation of $\alpha_D(O^+, T)$. We have obtained upper limits for $\alpha_D(S^+, 10^4\ K)$, $\alpha_D(Cl^{2+}, 10^4\ K)$ and $\alpha_D(Ar^{2+}, 10^4\ K)$ of 5.66×10^{-12}, 5.81×10^{-11} and 13.7×10^{-11} cm^3 s^{-1}, respectively. These correspond to low-temperature dielectronic recombination coefficients that are factors of 3.1, 17.5 and 42.5 higher than the corresponding radiative recombination rates for S^+, Cl^{2+} and Ar^{2+}, respectively. We also found that increasing $\alpha_D(O^+, T)$ by a factor of 3 yields a better fit to the [O II] spectrum. The very large rates required for Ar and Cl make it improbable that the discrepancies between the models and observations can be resolved solely in terms of these coefficients. This, together with the large ORL–CEL ADFs derived for NGC 1501, points to the existence of a second component, consisting of cold, metal-rich ORL-emitting knots. It seems that the solution to the overionization problem may lie partly with the softening of the ionizing radiation field, due to absorption of UV photons by such knots and partly with the lack/uncertainty of low-temperature dielectronic rates. Clearly, the magnitudes of the dielectronic rates required to fit the spectrum could be reduced by an amount depending on the fraction of the emitting gas comprised by the knots, as well as their size and density, which will affect the size of the shadowed regions.

We also note that NGC 1501 is yet another PN with a hydrogen-deficient central star that shows high ADFs. To our knowledge, NGC 1501, with its ADF of ∼32, has the third highest ADF of any nebula, after Abell 30 (ADF ∼ 700; Wesson et al. 2003) and Hf 2-2 (ADF ∼ 84; Liu 2003). Hydrogen-deficient knots are directly observed in the former (Jacoby et al. 1979; Hazard et al. 1980) and three-dimensional photoionization modelling (Ercolano et al. 2003b) has shown that in its case cold, metal-rich material can account for the ORL emission observed. In the case of Abell 30, a popular view with regards to the origins of such knots is the born-again scenario (Iben & Renzini 1983), whereby hydrogen-deficient material would have been stripped off the stellar surface during a late thermal pulse event.

There are, however, inconsistencies between the predictions of the born-again scenario and observations of some of the nebulae it applies to (including Abell 30). Most importantly, evolutionary models predict a late thermal pulse event to produce a carbon-rich stellar surface abundance (Herwig et al. 1999), whereas in the case of Abell 30, Wesson et al. (2003) measured $(C/O)_{orl} = 0.8$; similarly, for NGC 1501 we measured $(C/O)_{orl} = 0.31$. A reconciliation of theory and observations could be obtained if the ORLs were produced in a gas component consisting of carbon-rich material expelled from the stellar surface, which has already mixed somewhat with surrounding oxygen-rich nebular gas. In the case of a dense knot, one would expect the ionizing radiation to be able to penetrate only a thin outer layer, the same boundary region would also be the most likely to be subject to mixing. If the above is true, one would then expect the measured nebular $(C/O)_{orl}$ to be larger than $(C/O)_{cel}$, which is indeed confirmed by the data available in the literature. In particular, we looked at an ORL–CEL study of 16 PNe by Tsamis et al. (2004), for which 10 PNe had $(C/O)_{orl}/(C/O)_{cel} > 1$, two lacked a value for $(C/O)_{orl}$, two lacked a value for $(C/O)_{cel}$, and only for two PNe was $(C/O)_{orl}/(C/O)_{cel} < 1$. A similar trend is also confirmed by the work of Wesson (2004).

If the origin of the hydrogen-deficient knots can really be traced to material ejected from the surface of the AGB precursors of the central stars of born-again nebulae, one might also expect a correlation between hydrogen-deficient central stars and nebulae showing large ORL–CEL abundance discrepancies. Such a correlation did not emerge from investigation of the measured ORL–CEL ADFs (Liu et al. 1995, 2000, 2001b; De Marco & Barlow 2001; Liu 2003; Tsamis et al. 2004; Wesson 2004) and central star classification (e.g. De Marco & Barlow 2001) available in the literature. On the one hand, the central star spectral type is not always known and we cannot therefore exclude that some high-ADF central stars are not actually H-deficient. For instance, the spectral type of the central star of the PN Hf 2-2 (ADF = 84; Liu 2003) is unknown. On the other hand, the *IUE* spectra of the central star of PN DdDm 1 (ADF = 11.8; Wesson 2004) has no emission lines of C IV λ1550 or He II λ1640, which are expected in WR spectra. The jury is therefore still out as to whether or not the concept of H-deficient knots as an explanation for large ADFs can be reconciled with current post-AGB stellar evolutionary theories. We can, however, be certain that the high ADFs in nebulae such as NGC 1501 cannot be explained by nebular temperature fluctuations of the classically conceived type.

ACKNOWLEDGMENTS

We are grateful to Franco Sabbadin for providing the three-dimensional density distribution file of NGC 1501. We also thank

Pete Storey, Christophe Morisset and Falk Herwig for helpful discussions. We thank Lars Koesteke for providing model atmospheres, which account for NLTE, spherical expansion and metal line blanketing, and James Herald for the loan of the CMFGEN model atmosphere used for comparison with the Tübingen model. We thank Bob Rubin for helpful comments on the revised version and the anonymous referee for a thorough report. We acknowledge the Institute of Computational Mathematics and Scientific/Engineering Computing of the Chinese Academy of Science for the use of the PC cluster of the Major State Basic Research Project (973 project) 'Large Scale Scientific Computation', LSSC-I. BE and RW acknowledge support from PPARC. OD acknowledges financial support from Janet Jeppson Asimov. TR is supported by the DLR under grant 50 OR 0201.

REFERENCES

Acker A., 1978, A&AS, 33, 367
Ali B., Blum R.D., Bumgardner T.E., Cranmer S.R., Ferland G.J., Haefner R.I., Tiede G.P., 1991, PASP, 103, 1182
Allende Prieto C., Lambert D.L., Asplund M., 2001, ApJ, 556, L63
Allende Prieto C., Lambert D.L., Asplund M., 2002, ApJ, 573, L137
Aller L.H., 1976, Mem. Soc. R. Sci. Liege, 9, 271
Amnuel P.R., Guseinov O.K., Novruzova K.I., Rustamov I.S., 1984, Ap&SS, 107, 19
Barlow M.J., Hummer D.G., 1982, in de Loore C.W.H., Willis A.J., D. Reidel eds, IAU Symp. Vol. 99, Wolf–Rayet stars: Observations, Physics, Evolution. Astron. Soc. Pac., San Francisco, p. 387
Barlow M.J., Liu X.-W., Péquignot D., Storey P.J., Tsamis Y.G., C.M., 2003, in Dopita M., Southerland R., eds, IAU Symp. Vol. 209, Planetary Nebulae: their Evolution and Role in the Universe, Astron. Soc. Pac., San Francisco, p. 373
Beigman I.L., Chichkov B.N., 1980, J. Phys. B, 13, 565
Bond H.E., Ciardullo R., 1993, in Barstow M.A. ed., NATO Advanced Science Institutes (ASI) Series C. Vol. 403, White Dwarfs: Advances in Observation and Theory. Kluwer, Dordrecht, p. 491
Bond et al., 1996, AJ, 112, 2699
Cahn J.H., Kaler J.B., Stanghellini L., 1992, A&AS, 94, 399
Ciardullo R., Bond H.E., 1996, AJ, 111, 2332
Crowther P.A., de Marco O., Barlow M.J., 1998, MNRAS, 296, 367
Crowther P.A. et al., 2000, ApJ, 538, L51
De Marco O., Barlow M.J., 2001, Ap&SS, 275, 53
Drew J.E., Barlow M.J., Unruh Y.C., Parker Q.A., Wesson R., Pierce M.J., Mashder M.R.W., Phillipps S., 2004, MNRAS, 351, 206
Dudziak G., Péquignot D., Zijlstra A.A., Walsh J.R., 2000, A&A, 363, 717
Ercolano B., Barlow M.J., Storey P.J., Liu X.-W., 2003a, MNRAS, 340, 1136
Ercolano B., Barlow M.J., Storey P.J., Liu X.-W., Rauch T., Werner K., 2003b, MNRAS, 344, 1145
Feibelman W.A., 1998, ApJS, 119, 197
Gorny S.K., Stasinska G., 1995, A&A, 303, 893
Grevesse N., Sauval A., 1998, Space Sci. Rev., 85, 161
Grevesse N., Sauval A., 1999, A&A, 347, 348
Hazard G.H., Terlevich R., Ferland G., Morton D.C., Sargent W.L.W., 1980, Nat, 285, 463
Herwig F., Bloecker T., Langer N., Driebe T., 1999, A&A, 349, L5
Hillier D.J., Miller D.L., 1998, ApJ, 496, 407
Howarth I.D., 1983, MNRAS, 203, 801
Iben I.J., Renzini A., 1983, ARA&A, 21, 271
Jacoby G.H., 1979, PASP, 91, 754
Kaler J.B., 1976, ApJS, 31, 517
Kingdon J.B., Ferland G.J., 1995, ApJ, 442, 714
Kingsburgh R.L., Barlow M.J., 1994, MNRAS, 271, 257 (KB94)
Kingsburgh R.L., Barlow M.J., Storey P.J., 1995, A&A, 295, 75 (KBS95)
Koesterke L., Hamann W.-R., 1997, in Habing H.J., Lamers H.J.G.L.M. eds, IAU Symp. Vol. 180, Planetary Nebulae. Kluwer, Dordrecht, p. 114
Liu X.-W., 2002, in Henney W.J., Franco J., Martos M., Peñna. M., eds, Rev. Mex. Astron. Astrofis. Ser. Conf. Vol. 12, Ionized Gaseous Nebulae. UNAM, Mexico, p. 70
Liu X.-W., 2003, in Dopita M., Southerland R., eds, IAU Symp. Vol. 209, Planetary Nebulae: their Evolution and Role in the Universe. Astron. Soc. Pac., San Francisco, p. 373
Liu X.-W., Danziger I.J., 1993, MNRAS, 263, 256
Liu X.-W., Storey P.J., Barlow M.J., Clegg R.E.S., 1995, MNRAS, 272, 369
Liu X.-W., Storey P.J., Barlow M.J., Danziger I.J., Cohen M., Bryce M., 2000, MNRAS, 312, 585
Liu X.-W. et al., 2001a, MNRAS, 323, 343
Liu X.-W., Luo S.-G., Barlow M.J., Danziger I.J., Storey P.J., 2001b, MNRAS, 327, 141
Morisset C., Schaerer D., Bouret J.-C., Martins F., 2004, A&A, 415, 577
Nahar S.N., 1996, A&AS, 119, 509
Nussbaumer H., Storey P.J., 1984, A&AS, 56, 293
Peimbert M., 1967, ApJ, 150, 825
Peimbert M., 1971, Bol. Obs. Ton. Tac., 6, 29
Peimbert M., Torres-Peimbert S., 1983, Proc. IAU Symp. Vol. 103, Planetary Nebulae. Reidel, Dordrecht, p. 233
Peimbert M., Peimbert A., Ruiz M.T., Esteban C., 2004, ApJS, 150, 431
Péquignot D., Liu X.-W., Barlow M.J., Morisset C., 2003, in Dopita M., Southerland R., eds, IAU Symp. Vol. 209, Planetary Nebulae: their Evolution and Role in the Universe. Astron. Soc. Pac., San Francisco, p. 347
Ragazzoni R., Cappellaro E., Benetti S., Turatto M., Sabbadin F., 2001, A&A, 369, 1088
Rauch T., 2003, A&A, 403, 709
Rubin R.H., 1968, ApJ, 153, 761
Rubin R.H., 1986, ApJ, 309, 334
Rubin R.H., Simpson J.P., Erickson E.F., Haas M.R., 1988, ApJ, 327, 377
Ruiz M.T., Peimbert A., Peimbert M., Esteban C., 2003, ApJ, 595, 247
Sabbadin F., Hamzaoglu E., 1982, A&AS, 50, 1
Sabbadin F., Benetti S., Cappellaro E., Turatto M., 2000a, A&A, 361, 1112
Sabbadin F., Cappellaro E., Benetti S., Turatto M., Zanin C., 2000b, A&A, 355, 688
Stanghellini L., Kaler J.B., Shaw R.A., 1994, A&A, 291, 604
Storey P.J., Hummer D.G., 1995, MNRAS, 272, 41
Tsamis Y.G., Barlow M.J., Liu X.-W., Storey P.J., Danziger I.J., 2004, MNRAS, in press (doi:10.1111/j.1365-2966.2004.08140.x)
Tylenda R., 2003, in Dopita M., Southerland R., eds, IAU Symp. Vol. 209, Planetary Nebulae: their Evolution and Role in the Universe, Astron. Soc. Pac., San Francisco, p. 389
Tylenda R., Acker A., Stenholm B., 1993, A&AS, 102, 595
Werner K., Heber U., Hunger K., 1991, A&A, 244, 437
Wesson R., 2004, PhD thesis, Univ. London
Wesson R., Liu X.-W., Barlow M.J., 2003, MNRAS, 340, 253
Zhang H.L., 1996, A&AS, 119, 509

This paper has been typeset from a TEX/LATEX file prepared by the author.